2011

Effects of Thermo-mechanical Loading From In-situ Studies of EB-PVD Thermal Barrier Coatings

Melan N. Jansz
University of Central Florida

EFFECTS OF THERMO-MECHANICAL LOADING FROM IN-SITU STUDIES OF EB-PVD THERMAL BARRIER COATINGS

by

Melan N. Jansz
B.S. University of Central Florida, 2008

A thesis submitted in partial fulfillment of the requirements
for the degree of Master of Science
in the Department of Mechanical, Materials and Aerospace Engineering
in the College of Engineering and Computer Science
at the University of Central Florida
Orlando, Florida

Summer Term
2011

Major Professor:
Seetha Raghavan

Abstract

The thermo-mechanical effects on the strain evolution within an EB-PVD thermal barrier coating (TBC) is presented in this work using in-situ characterization. Synchrotron X-ray diffraction at sector 1-ID at the Argonne National Laboratory provided both qualitative and quantitative in-situ data on the strain evolution under a thermal cycle with mechanical loading. The results show that at a critical combination of temperature and load, the stress in the thermally grown oxide (TGO) layer in the TBC reaches a tensile region. These significant findings enhance existing literature showing purely compressive strains within the TGO where mechanical loads have been neglected. The results have important implications on the effects on the overall life of the coating. Depth resolved quantitative strain is presented as contour plots over a thermal cycle highlighting the complementary strains in the adjacent layers including the bond coat and the TBC with time and temperature. Systematic identification of the appropriate peaks within the multi-layer TBC system provides guidelines for future strain studies using high energy X-rays. Piezospectroscopic studies with applied mechanical loading are further presented as verification of the room temperature XRD data for future development of the method as an operational technique to be used outside the laboratory environment.

This work is dedicated to my loving parents and two brothers whose endless support helped me get to where I am today.

Acknowledgments

I would first like to thank my advisor and thesis Chair, Dr. Seetha Raghavan, for her boundless support, guidance, and encouragement throughout the entirety of this project. My sincere gratitude is offered to Dr. Jayant Kapat and Dr. C. Suryanarayana for their expertise and advice, making this project a success. I am also thankful to Dr. Jonathan Almer and Dr. John Okasinski at Argonne National Laboratory (ANL) for their help on using the equipment at ANL and also their great advice and insights on XRD data analysis along with the provision of the programs essential towards the success of this project. Great appreciation is also given to the following University of Central Florida students for their combined assistance with the discussions, experiments, and data analysis: Rene Diaz (Undergraduate, Mechanical Engineering), Mitra Mossaddad (Undergraduate, Aerospace Engineering), Talia Field (Undergraduate, Mechanical Engineering), Amanda Stevenson (Graduate, Mechanical Engineering), Bharathi Mohan (Graduate, Mechanical Engineering), Gregory Freihofer (Graduate, Aerospace Engineering), and Ashley Jones (Graduate, Mechanical Engineering). This work was funded by the Florida Center for Advanced Aero-Propulsion (FCAAP). The use of the Adavanced Photon Source at Argonne National Laboratory (ANL) supported by the U. S. Department of Energy, Office of Science, Office of Basic Energy Sciences, under Contract No. DE-AC02-06.

TABLE OF CONTENTS

LIST OF FIGURES

LIST OF TABLES

CHAPTER 1
INTRODUCTION

1.1 Motivation and Background

For the last few decades, thermal barrier coating (TBC) systems have served immensely towards protecting the blade section of a turbine from high operating temperatures. Their presence allows for the operation of turbines at very high entrance temperatures and with reduced internal cooling requirements, thereby contributing to the overall efficiency of the engine [6, 1, 7].

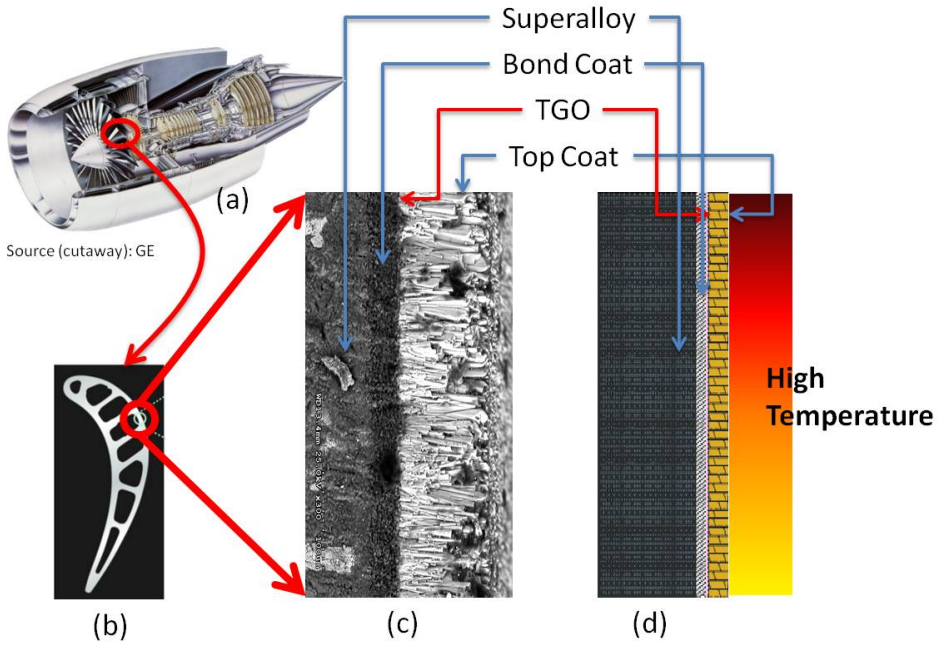

Figure 1.1: (a) Cutaway view of a jet engine. (b) Cross section of a turbine blade from a jet engine. (c) SEM image of the coating on the surface of the blade (d) Schematic of the layers of the TBC coating system

Figure 1.1 presents an SEM image of the thermal barrier coating system providing protection to the nickel super-alloy blade section.

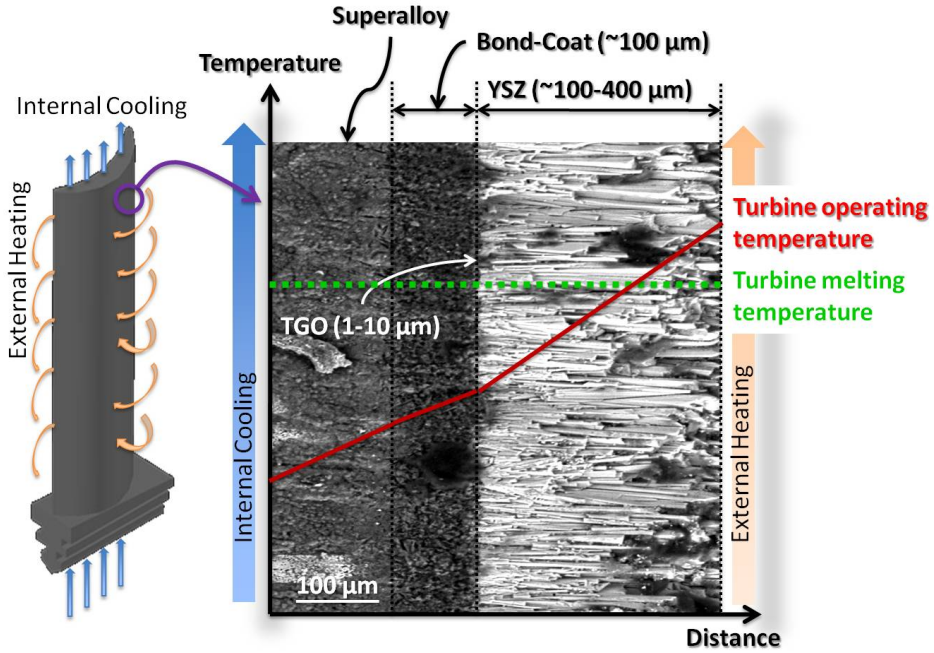

Figure 1.2: Cross-sectional scanning electron micrograph (SEM) of an electron-beam physical-vapor deposited (EB-PVD) TBC, superimposed onto a schematic diagram showing the temperature reduction provided by the TBC.

As illustrated in Figure 1.2, a TBC system consists of a ceramic Yttria-Stabilized Zirconia (YSZ) topcoat which contains Zirconium Yttrium Oxide (ZrO_2+Y_2O_3) and this layer is adhered to the surface of the nickel supper-alloy substrate by an oxidation-resistant Nickel Aluminide (NiAl) based bond-coat. Due to the initial thermal mismatch and the thermal cycles the system experiences, an oxide layer α-alumina ($\alpha - Al_2O_3$), also known as the thermally grown oxide (TGO) layer, develops between the YSZ and the bond coat. These top coats are known for their excellent low thermal conductivity

Table 1.1: Material properties for the different layers of the TBC system [4, 5]

Property	Superalloy	Bond Coat	TGO	YSZ
Poisson's Ratio	0.31-0.35	0.30-0.33	0.23-0.25	0.23-0.25
Elastic Modulus (GPa)	120-220	110-200	320-400	100-220
Thermal Expansion Coefficient ($10^{-6}/^{0}C$)	14.8-18.0	13.6-17.6	8.0-9.6	9.0-12.2

and higher heat capacity [6, 8, 9] which serves well on the efficiency of turbines and the Table 1.1 provides the material properties for each of these different layers.

The YSZ topcoats are deposited on the nickel substrate using different methods such as air plasma spray (APS) or electron beam-physical vapor deposition (EB-PVD). In the APS method, a coating material is melted and propelled towards a substrate. There, the molten droplets flatten, rapidly solidify and form a deposit attached to the substrate as a coating. In the EB-PVD method, a target anode is forced to react with an electron beam produced by a charged tungsten inside a vacuum. This reaction produces a gaseous form of the target anode and this gas solidifies on top of the surface to create a coating. These two methods leave distinctively different microstructures for the coating [7, 10] as illustrated in Figure 1.3. The top coat also referred to as the YSZ layer which results from the EB-PVD method has a significant columnar structure distinctive from the APS method. This research was focused on the coatings produced by the EB-PVD method which is used predominantly on jet engines.

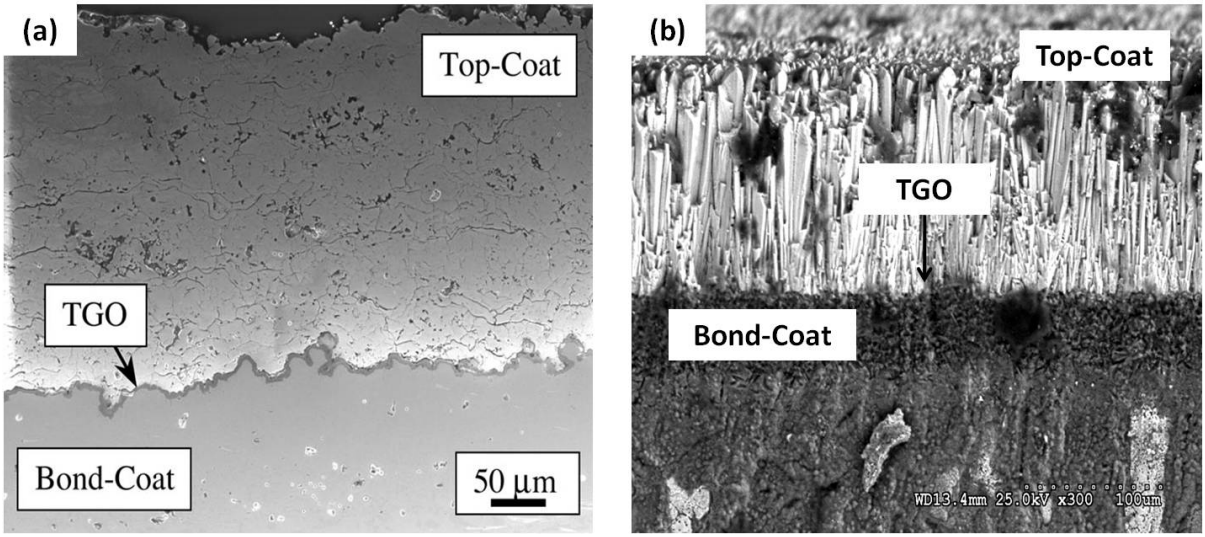

Figure 1.3: Comparison of the microstructure: (a) SEM image of an APS coating system [1]. (b) SEM image of an EB-PVD coating system used in this research

TBC systems from jet engine turbine blades are exposed to some of the harshest conditions such as high temperature cycling, centrifugal loads and also environmental effects such as sand and volcanic ash contamination. To overcome these conditions, TBCs are engineered with a complex and dynamic intermix of high temperature ceramics and metals, layered topology and oxide formation as discussed before. Even though these factors serve the purpose of blade protection to a great extent, sometimes the very same characteristics cause the degradation and eventual failure by spallation of the top coat, exposing the nickel superalloy to the unfavorable high temperature [11, 12, 13]. Over the last decade, progress in the understanding of the TBC systems has been made through studies of pre-cycled coated specimens to illustrate the various stages of the coating

life [14, 15, 16, 17, 18]. These *ex-situ* studies were mainly focused on the high compressive stress mainly in the TGO layer and how that could lead to phenomena such as spallation of the topcoat. Another hypothesized phenomenon is the effect of the out of plane growth stresses of the undulated oxide layer which takes place during the thermal cycle. This undulated nature of the oxide when modeled in computational studies, reveal significant out of plane stresses [4, 5] that can only be verified with *in-situ* studies. Since this is a poorly understood scenario it demands the need for experimental *in-situ* studies to track the oxide growth and behavior during a cycle.

1.2 In-situ strain measurements of thermal barrier coatings using synchrotron X-ray diffraction

There have been studies by Veal et al. [16, 19] where they obtained synchrotron XRD readings from oxide formation on an FeCrAlY substrate during a cycle. Almer et al. [20] also investigated internal strain and crystallographic orientation (texture) in physical-vapor deposited metal nitride coatings of TiN and CrN to obtain strain and intensity distributions of multiple crystallographic planes by a single X-ray exposure and they also investigated oxide strain during oxide formation on a Kanthal Al FeCrAlZr substance at 1160^0C [21]. In these studies, *in-situ* measurements of Debye-Scherrer diffraction patterns from the scale were recorded during oxidation and cooling, and the elliptical distortion of the diffraction rings was analyzed to yield the in-plane strain.

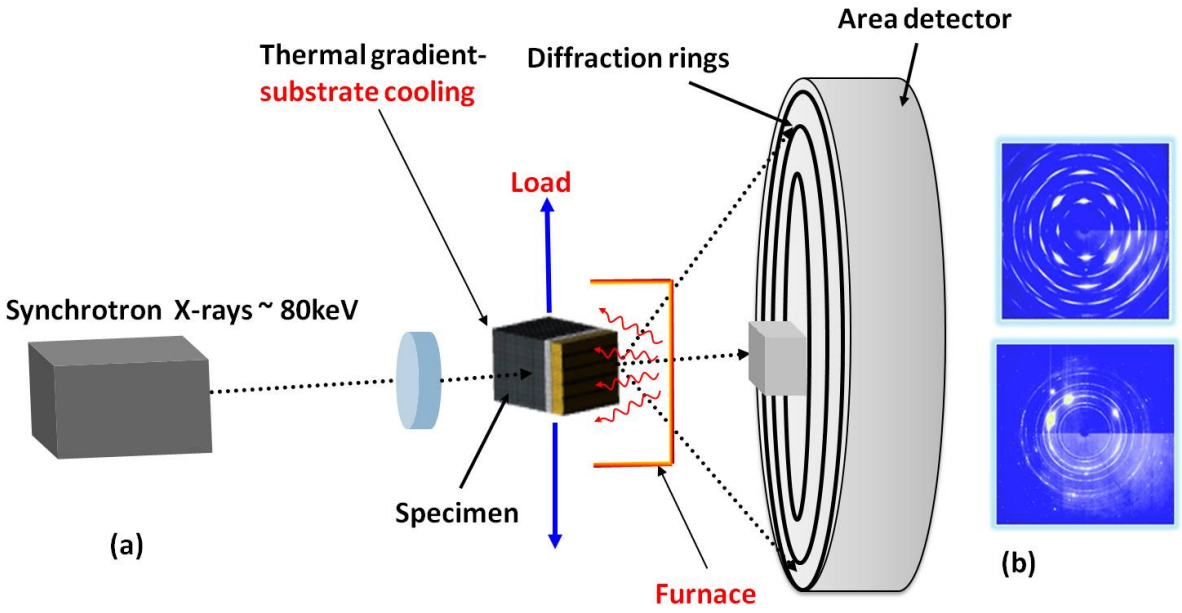

Figure 1.4: (a) Schematic of an *in-situ* data collection of a TBC specimen while under thermo-mechanical loading (b) sample Debye-Scherrer diffraction patterns

In their studies, Veal et al. verified large tensile strains occurring within the early oxide as the oxide undergoes a phase change and associated volume reduction. However, these in-situ measurements were performed in the absence of a TBC top coat. Such studies provided motivation for this research on TBC strain analysis where the complete TBC system including the YSZ top coat was considered.

The effectiveness and usefulness of using high energy X-rays, are reinforced by *in-situ* studies on other systems other than TBCs where synchrotron X-ray diffraction has been used [22, 23, 24] with outstanding results merely due to its high resolution. Ex-situ studies at synchrotron facilities have been applied to TBC specimens including depth profile of strain on pre-cycled plasma-sprayed TBC specimens [25, 26, 27, 28, 29] revealing the variation of the strain across the layers. Thornton et al. [27, 28] used synchrotron X-rays to successfully analyze the depth resolved residual stresses of a super-alloy coated with zirconia identifying the maximum compressive stress in the TGO layer in both heated and unheated samples and the out-of-plane tensile strains in the zirconia layer. Gelfi et al. [25] considered residual stresses to be difficult to predict and hence used XRD due to its high spatial resolution, proving it to be a suitable method for stress analysis of coatings and other samples with complex geometries. Weyant et al. [29] also used high energy X-rays to determine the local phase composition and residual stress in a heat treated TBC coating and this study revealed the effects of the TGO and the segmentation cracks on the in-plane stress of the entire coating. All these studies show the benefits of using high

resolution methods such as synchrotron X-ray diffraction to obtain necessary information on TBC systems.

This current research focuses on *in-situ* measurements of TBCs during a thermo-mechanical cycle using synchrotron XRD to analyze the strain evolution of the whole depth profile of the TBC system.

1.3 Consideration of the Mechanical loading due to centrifugal force of a turbine on the TBC system

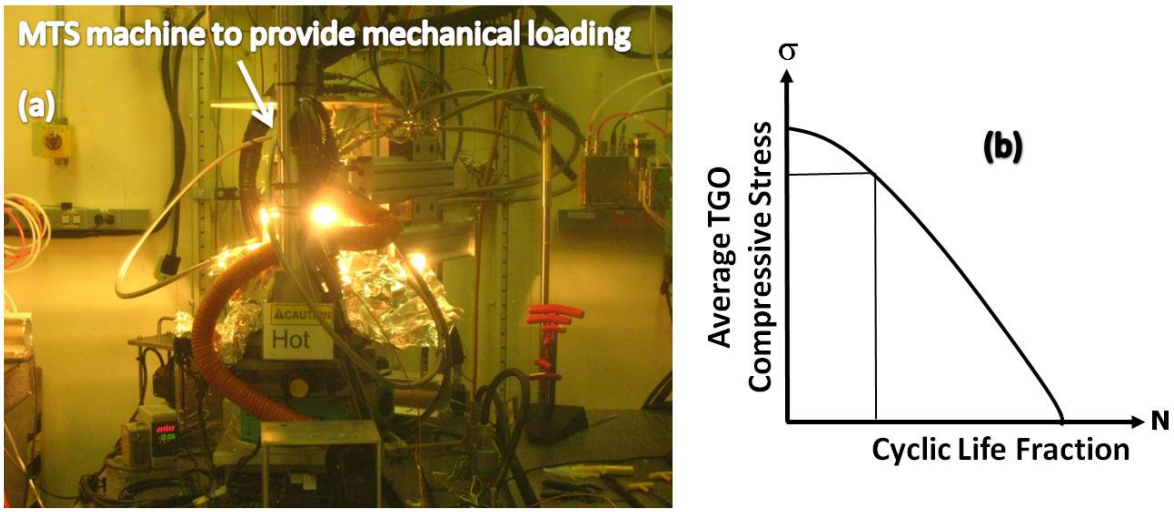

Figure 1.5: (a) In situ thermo-mechanical testing at Sector 1-ID-C, Advanced Photon Source, ANL (b) Schematic of a stress-life graph which can be used to predict the life fraction of a TBC system

Researchers conducting studies to evaluate the life of a single crystal nickel-based super-alloy under thermo-mechanical fatigue (TMF) loading have in some cases included the effect of coatings to find that the interaction between the oxidation and fatigue cracking seems to play a major role in the blade life [30, 31, 32, 33]. However there are limited studies considering the effect of mechanical loading on the TGO strains and subsequently on the life of the coatings. Recent work by Kitazawa et al. [34] evaluated the damage of a TBC system under thermo-mechanical tests where failure after cycling was observed using optical microscopy. In thermal mechanical fatigue tests with controlled thermal gradients conducted by Bartsch et al. [35], cracks parallel to the surface were observed and attributed to effects of the mechanical loading. Therefore mechanical loading is potentially an important factor to consider when analyzing the behavior that leads to failure within the TBC coating system and this serves as the motivation for this work. Here, an in-situ approach allows for the effect of the mechanical loading to be captured during a cycle. Such a study was made possible as illustrated in Figure 1.5 using a MTS load cell while the specimen was under a thermal cycle. This experiment was performed at Sector 1-ID at the Advanced Photon Source (APS) at Argonne National Laboratory (ANL). By obtaining strain measurements including the effects such as thermo-mechanical loading and by collecting *in-situ* data with a high resolution XRD method, it will be possible to closely simulate the operational conditions of the TBC system.

1.4 Piezospectroscopy in TGO stress measurement

Piezospectroscopy (PS) is an effective operational technique for stress measurement and has gained significance in TBC integrity studies. Here, a shift in characteristic spectral peaks gives a direct correlation to the stress present in polycrystalline alumina that forms the TGO layer in the TBC system. These spectral lines are also referred to as the R-lines. Barnett et al. [36] studied R1 line to monitor pressure in diamond anvil cells and this trend followed by using Photo-stimulated luminescence spectroscopy (PSLS) to determine the stresses in polycrystalline material [37, 38, 39]. Studies have proved this method effective to determine stress in the TGO layer of the TBC [17, 40, 41, 42].

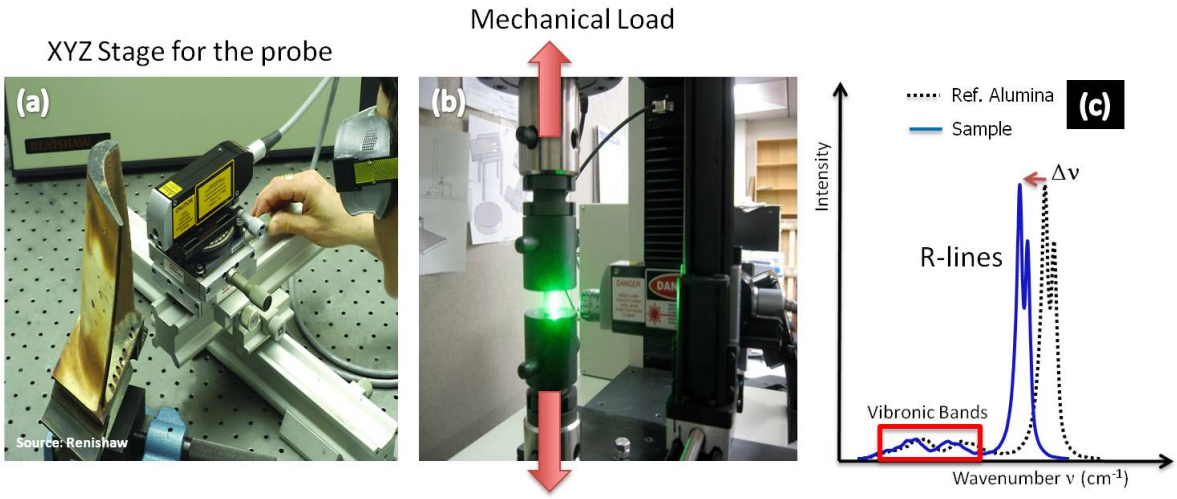

Figure 1.6: (a) XYZ stage used with the probe to obtain PS data (b) In-house setting of the mechanical load setting at the UCF lab (c) PSLS method in use to obtain the stress of a polycrystalline material

While all these studies have been *ex-situ* in nature, they have provided a wealth of information. Compared to the information on crystallographic structure and morphology, which could be achieved by XRD method, PSLS reveals information on molecular bond energies and orientations of the system, offering the ability to establish oxide stresses non-invasively and outstanding itself as an operational technique. PSLS method was used in this research to compare with the XRD results taken under room temperature for different loading conditions to investigate the worthiness of the technique with respect to its resolution. As illustrated in Figure 1.6 the laboratory at University of Central Florida (UCF) has the facility to conduct such an experiment in-house. The design of the optical stress probe system was described in the work by Friehofer et al. [43] at UCF and this laser probe was connected to a Raman Spectroscopy equipment to obtain and analyze the R-lines as the sample undergoes mechanical loading.

1.5 Overview of the research

The individual importance of considering external mechanical loads on the TBC behavior and *in-situ* studies on the evolution of strains within a cycle has been presented in the earlier sections. Therefore a combination of these factors where in-situ synchrotron X-ray diffraction collects depth-resolved high resolution strain measurements during a thermo-mechanical cycle would potentially provide a wealth of information for TBC life prediction. In addition, the potential of PSLS as an operational technique for stress and

integrity assessment of the TBC system motivates the need to advance this method using synchrotron XRD measurements for comparison.

Chapter 2 will focus on the initial stage of the synchrotron X-ray diffraction study which involves characterizing the diffraction rings and identifying the peaks in different lineout plots obtained as a result of integrating those diffraction rings. First, a theoretical background on synchrotron X-ray diffraction and its use will be provided. Then, an application on tri-modal Metal Matrix Composite (MMC) will be presented, mainly using the findings to give a good understanding about the peak identification process used. A step by step approach will be presented to identify most of the unknown peaks from a given lineout plot based on the knowledge provided about the possible materials and compounds in the composite. Also the method of using the identified peaks to analyze the grain growth in MMC will be discussed. This approach is extended to identify peaks in a set of lineout plots obtained for a TBC system. For the research done on the TBC system, it was important to identify the data which corresponds to the TGO layer to focus more on the strain in this layer separately. The fitting process to determine the strain from the diffraction data will be explained.

Chapter 3 will discuss the effect of the thermo-mechanical loading on the TBC strain while using XRD measurements. First, this chapter will give an overview of the XRD experimental procedure in this research to obtain the results, such as sample preparation and the experimental setup at Argonne National Laboratory. The results showing the effect of mechanical loading on the overall strains within the TBC system will be

presented. These results will show that at a critical combination of temperature and mechanical loading the strain in the TGO layer will reach a tensile region. Results of the evolution of the strain throughout all the layers in the TBC system during a cycle will be presented. Final discussion will include a qualitative discussion of the impact of the results on the life cycle of the TBC system.

Chapter 4 will present stress measurements using Photo stimulated luminescence spectroscopy (PSLS) method with a comparison of the XRD results obtained during room temperature under different mechanical loading conditions. The main objective in this chapter will be to assess the PSLS method for measurement of stresses and the needs for resolution improvement. This method is of interest for development as an operational technique since it is not plausible to use synchrotron XRD techniques in a typical field environmental despite its reliability of high resolution data collection.

CHAPTER 2
CHARACTERIZING SYNCHROTRON XRD PEAKS IN CERAMIC COMPOSITE MATERIALS

2.1 Theory on synchrotron X-ray diffraction

X-ray diffraction (XRD) is a method to identify and characterize the atomic structure of materials and the governing theory behind this process is defined by Bragg's law. In XRD, an X-ray beam interacts with a sample, scattering according to the structure of the material. This scattering will result in different powder diffraction rings for different materials of a polycrystalline nature. Figure 2.1 illustrates Bragg's law.

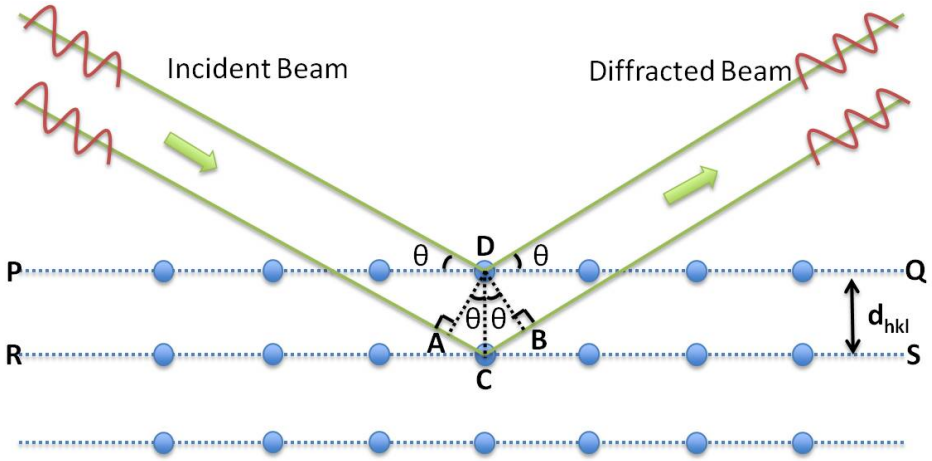

Figure 2.1: Incident X-ray beams reflects according to the structure of the atomic planes

PQ and RS are two parallel planes of atoms with the same Miller indices and separated by the inter-planer spacing d_{hkl}. As illustrated in the Figure 2.1, two rays of the incident beam with a wavelength λ meet these two planes at an angle θ. These rays are scattered by the atoms C and D and this diffracted beam takes an angle θ as well. If the difference

between the two paths of the two different beams is equal to a whole number, n, of wavelengths then according to the Figure 2.1,

$$n\lambda = AC + CB \tag{2.1}$$

Then using trigonometry,

$$n\lambda = d_{hkl}\sin\theta + d_{hkl}\sin\theta \tag{2.2}$$

$$n\lambda = 2d_{hkl}\sin\theta \tag{2.3}$$

Equation 2.2 is known as Bragg's law where n is the order of reflection. Mostly Bragg's law is associated with the first order for n which simplifies the equation to

$$\lambda = 2d_{hkl}\sin\theta \tag{2.4}$$

In this research using XRD, the peaks were identified for different materials in order to analyze the strains and also the grain sizes of the material. Among existing methods to investigate coating stress and strain, X-ray diffraction is a powerful tool due to its capability to measure the full strain/stress tensor and provide complementary texture and crystallographic phase information nondestructively [20]. In synchrotron X-ray diffraction, a high energy X-ray beam penetrates the sample and the beam diffracts according

to Bragg's law. A photo sensitive device will capture the scattered beam in a form of a set of rings as illustrated in part (b) of the Figure 2.2, which shows the transmission setup used in the experiment.

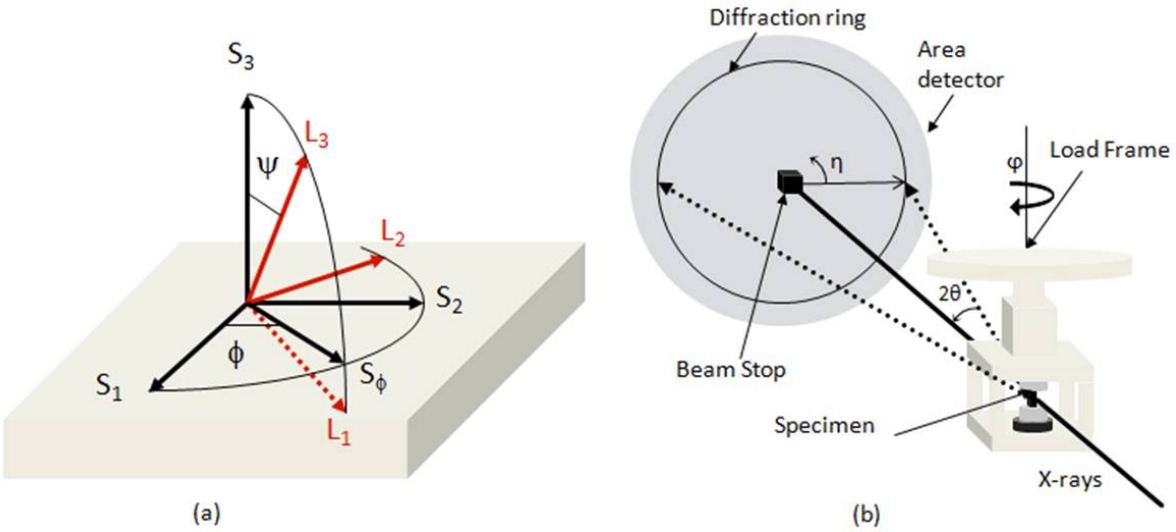

Figure 2.2: (a) Coordinate systems of the laboratory setup Ł$_i$ and the sample setup S_i shown in reflection geometry (b) Scattering of the incident beam due to the atomic structure of the sample [2] shown in transmission mode.

These rings correspond to different crystallographic planes of the sample material. These diffraction patterns were azimuthally integrated and converted into lineout plots using a MATLAB-based analysis program provided by Sector 1-ID of the Advanced Photon Source, Argonne National Laboratory. The method of analysis is described in more detail in the Appendix C. These lineout plots will have the d-spacing for the x-axis and the intensity for the y-axis. Figure 2.3 illustrates an example diffraction pattern for

the multilayer TBC sample and the resulting lineout plot of the inner most ring of the diffraction pattern. This corresponds to the furthest peak in the lineout plot since the radius of the diffraction ring has an inversely proportional relationship to the d-spacing in the lineout plot.

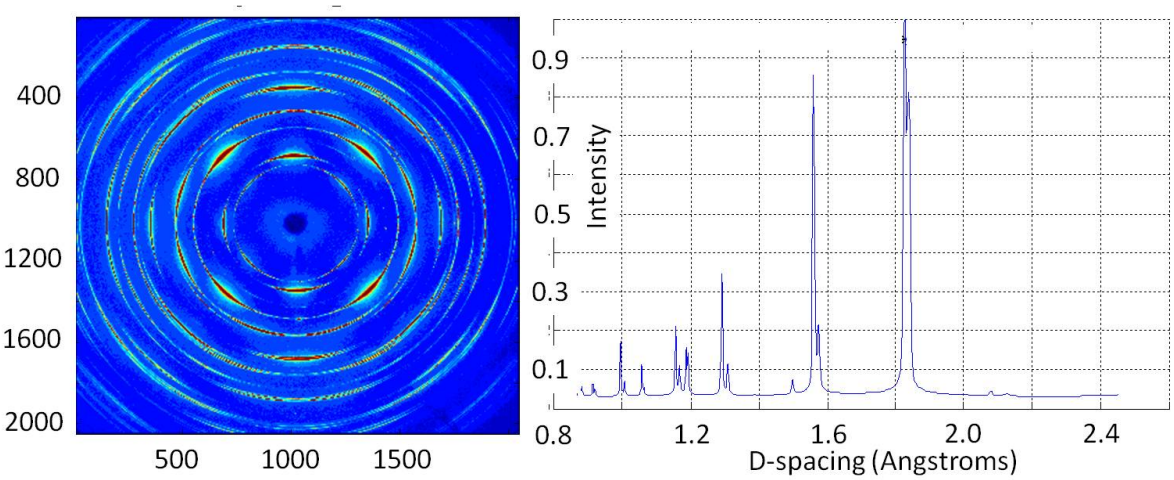

Figure 2.3: 2D raw image of the diffraction rings from a TBC sample and the corresponding lineout plot

These different peaks correspond to different materials within the layers and the location of the reading. Identifying the correct peak is the most crucial step in the process of characterizing XRD peaks especially in composite material systems. Using the database provided by the Joint Committee on Powder Diffraction Standards (JCPDS) of the International Center for Diffraction Data (ICDD), for known materials, these peaks could be distinguished and the systematic method follows for the identification of the peaks. The database presents tables with the corresponding 2θ values, d-spacing values,

relative intensity and also the corresponding hkl values. Table A.1 in the Appendix is an example of such data for the main peaks of Alpha alumina ($\alpha - Al_2O_3$), which would be considered when analyzing the strains in the TGO layer of the TBC system. In the following sections, the identification of peaks and characterization of grain-size in thermo-mechanical studies of ceramics-based metal matrix composites are presented. The knowledge gained from this work was applied to identifying peaks in the multilayer TBC system and presented here along with the characterization method for strain in these layers.

2.2 Use of synchrotron X-ray diffraction on Metal Matrix Composites

Tri-modal Aluminum Metal Matrix Composites (MMCs) consisting of a nano-crystalline Al phase (NC-Al), boron carbide (B_4C) reinforcement particles, and a coarse-grain Al phase (CG-Al) has been successfully fabricated and are considered to have superior strength, low density, and high corrosion resistance.

Table 2.1: Different cryomilled times for the different powder samples

Powder Sample	Contents	Cryomill Time (Hours)
Powder 1	Al 5083	0
Powder 2	Al 5083 + B_4C	4
Powder 3	Al 5083 + B_4C	8
Powder 4	Al 5083 + B_4C	24

The manufacturing process blends commercial gas-atomized Al 5083 with B_4C powders using a cryomilling process under liquid nitrogen atmosphere for up to 24 hours. Extrusion, forging, and rolling are then used to produce a bulk material [44, 45, 46]. In an attempt to quantify how the thermo-mechanical manufacturing process influences the properties of MMCs, this work will introduce the X-ray diffraction experiments performed at Argonne National Laboratory and detail the analysis of the nano aluminum grain size as a function of temperature and strain. The experiments and analysis were performed to identify the peaks and to determine the grain size evolution in the MMC.

Table 2.2: Different experimental conditions for different MMC samples

MMC Sample	External Compressive Stress (MPa)	Temperature(^0C)
Sample 1	100	300
Sample 2	100	200
Sample 3	100	400
Sample 4	200	200
Sample 5	50	200
Sample 6	50	25-400 ramped up with 5 increments
Sample 7	50	300
Sample 8	N/A	N/A
Sample 9	25	300
Sample 10	25	200

The experimental setup, consisted of an MTS machine which was mounted on an XYZ stage for mobility, a specimen table where the specimen was placed, a GE detector with a lead stop to impede the transmitted X-ray beam, and a furnace positioned around the specimen similar to that shown in Figure 3.3. In this case, the samples were given a compressive loading. Four powders were tested including aluminum alloy 5083 powder and Al 5083 with B_4C at three different cryomill times as shown in Table 2.1. These powders were analyzed by placing the material in the space of a small washer and placing a clear tape on both sides to keep the powders in position. The tape was verified to have no effect on the diffraction results due to the disproportionate volume fractions of tape and powder.

MMC specimens with right prism dimensions were tested under different thermo mechanical conditions with combinations of stresses which corresponds to loads of 25, 50, 100, and 200 MPa and temperatures of 200, 300, and 400^oC as shown in Table 2.2. Once a specimen was placed on the MTS machine and leveled to be perpendicular to the incident beam, reference measurements were taken for both conditions: unloaded at room temperature and loaded at room temperature for all specimens. While mechanically loaded, the furnace was set for the designated temperature. Measurements of the thermo mechanical load commenced once the desired temperature was achieved and stable.

2.2.1 Peak identification using synchrotron XRD data for Metal Matrix Composites

The results of the XRD experiments are presented here. The manufacturing process of the MMCs results in the formation of compounds which have been identified through the synchrotron results in this work. This enables an understanding of the change in composition of the material and hence helps to assess the effects of the manufacturing process on the mechanical properties of the material.

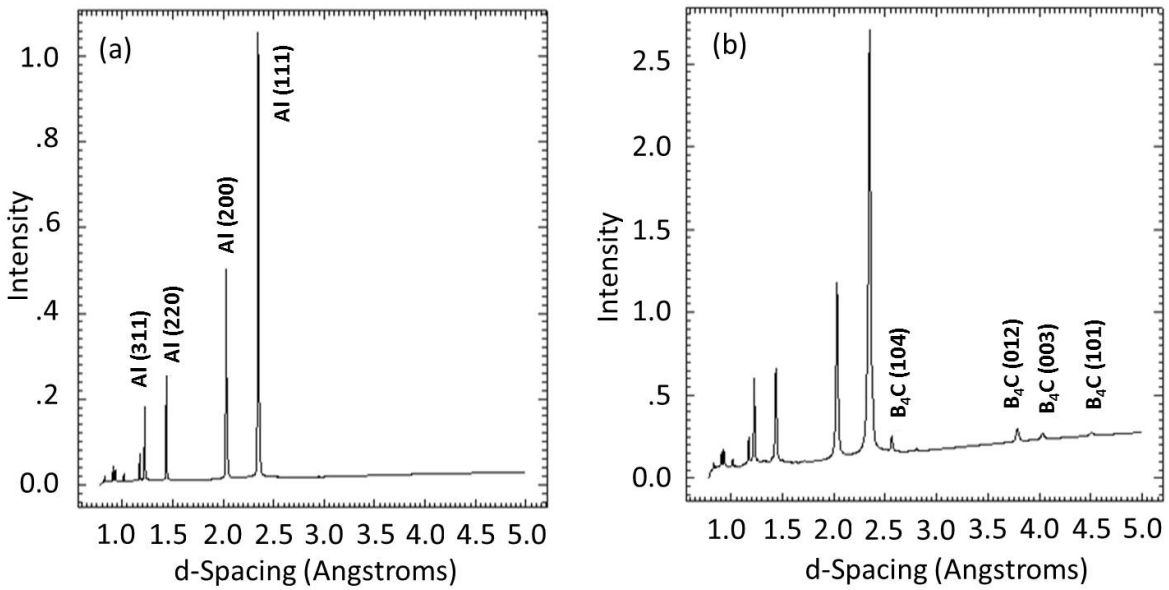

Figure 2.4: (a) Lineout plot of the non-cryomilled sample. (b) Lineout plot of the 24-hour cryomilled sample

The MMC powder samples investigated were mainly composed of Aluminum (Al) and Boron Carbide (B_4C). Thus, phase identification of these components was the first step.

Figure 2.4 shows two XRD lineout plots, produced from the experimental data using the analysis procedure, where one of the plots represents the non-cryomilled sample with pure aluminum and the next plot represents a composite sample cryomilled for 24 hours. It is evident that there are additional peaks in the latter compared to the former. Figure 2.4 (a) depicts the lineout plot for the pure Al 5083 powder before it was mixed with B_4C. Several main Al peaks are identified according to the JCPDS for centro-symmetric Al which is included in Table A.2 in the Appendix. According to the table, the Al peak with the highest intensity is the (111) peak identified at a d-spacing of 2.338 $\mathring{A}$ on the lineout and the next peak with the high intensity is the (200) peak at 2.024 $\mathring{A}$ on the lineout. The intensity ratio between these two peaks is approximately 2 according to the table and this must be verified when identifying a peak. According to Figure 2.4 (a) there are two peaks closely at 2.338 $\mathring{A}$ and at 2.024 $\mathring{A}$ with intensities of 3800 and 2000 respectively. Therefore since these two peaks correspond well to the d-spacing values and the intensity ratios of the expected two peaks, it was confirmed that these are the correct Al peaks as assumed. Using the same method, other main Al peaks could be identified according to the d-spacing value and the intensity compared to the intensity of an already identified peak. The lineout plot for the Al 5083 powder with B_4C after 24 hours of cryomilling shown in Figure 2.4 (b) was examined. The B_4C peaks are identified as shown in Figure 2.4 (b). Comparison between XRD data of varying cryomilling times between 4, 8, and 24 hours showed insignificant changes. Thus, the conclusion was made

that at the end of the 24 hour cryomilling process, only Al and B_4C formed the main compounds present within the sample.

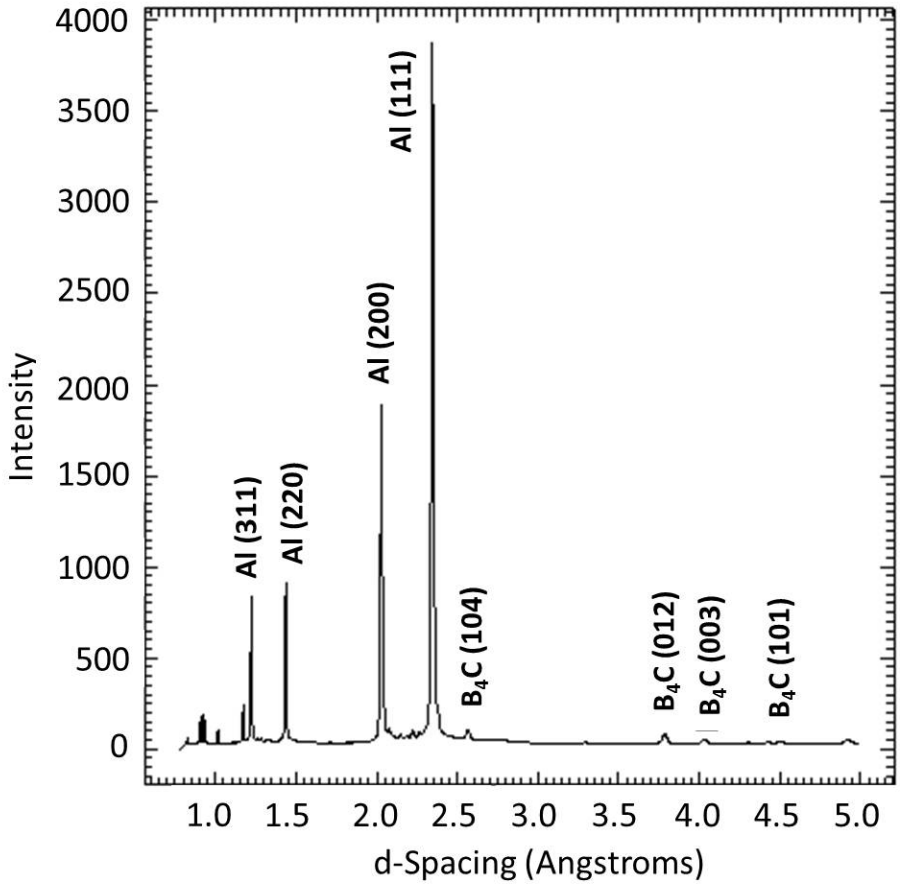

Figure 2.5: Lineout plot of the unloaded MMC sample at room temperature with the initially identified peaks.

The presence of compounds such as Aluminum Nitride (AlN) from the cryomilling process which takes place under liquid nitrogen atmosphere was not detected at this point. However, AlN peaks were identified subsequent to the manufacturing process. It is deduced that following the cryomilling process, the secondary manufacturing pro-

cess (forging, rolling, and extrusion) results in the formation of sufficient quantities of these compounds for identification. The presence of impurities such as Al_2O_3, AlN, and Al_4C_3 is of significance because these will contribute additionally to the exceptional high strength of the composite [45].

After the main Al and B_4C peaks were identified in the powder of the MMC as seen in Figure 2.4, the bulk material (sample at room temperature and no load) was examined and the corresponding lineout plot for this sample is shown in Figure 2.5. Since it was determined before that there is Al present in the sample, all the Al peaks must be evident throughout the plot and these can be identified by analyzing the different parts of the lineout plot. One of the expected by-products of the cryomilling process is AlN, which has 2 crystal structures, namely Centro-symmetric and Non-centrosymmetric. When all of the corresponding d-spacing values for the Centrosymmetric AlN peaks were examined, it was determined that these peaks were overlapped by Al peaks. When the Non-Centrosymmetric peaks were examined, one of the peaks was evident.

Figure 2.6 is the zoomed in view of the lineout plot of the unloaded MMC sample at room temperature from 1.0$\mathring{A}$ to 1.5 $\mathring{A}$ and it identifies three B_4C peaks and four Al peaks according to the JCPDS for centrosymmetric B_4C and Al considering the d-spacing and the relative intensities provided. For example, according to the JCPDS for centrosymmetric B_4C, the peak with the highest intensity is (104) which is at 2.5800$\mathring{A}$. Another prospective peak within the range 1-1.5 $\mathring{A}$ is (220) which is at 1.3995$\mathring{A}$ and these two peaks are supposed to have a relative intensity of 5.3:1 respectively. Figure 2.5

already has the peak (104) identified and when the intensity of this peak was compared to the (220) peak intensity it matched the relative intensity expected which allowed to confirm (220) peak position.

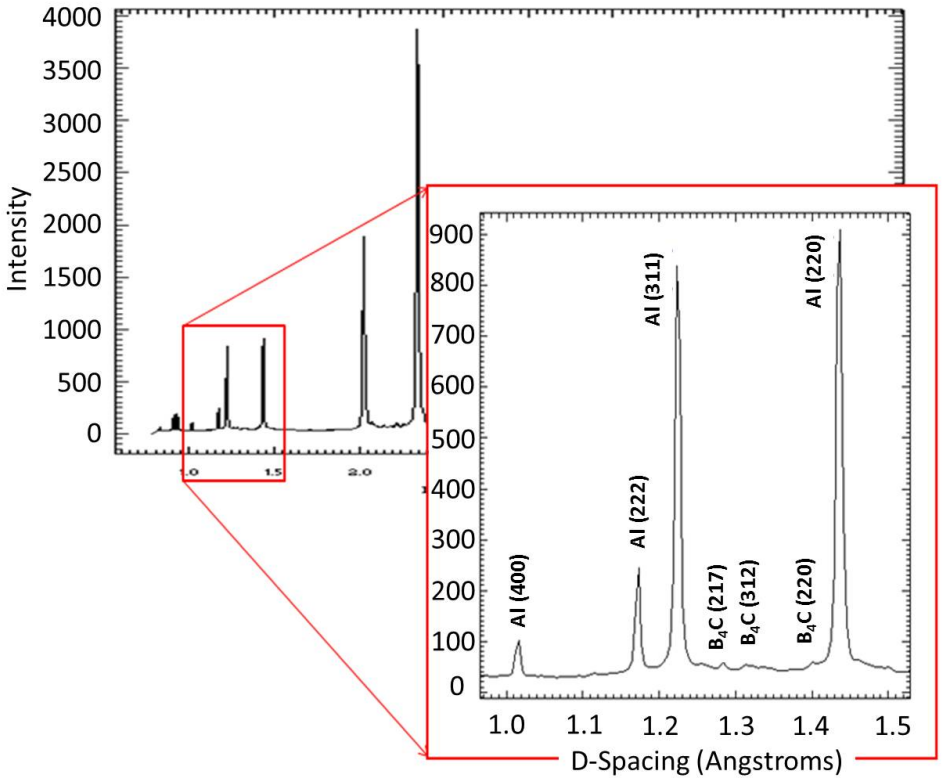

Figure 2.6: Zoomed in view of the lineout plot of the unloaded MMC sample at room temperature from 1.0$\mathring{A}$ to 1.5 $\mathring{A}$

Figure 2.7 is the zoomed in view of the lineout plot of the unloaded MMC sample at room temperature from 2.0$\mathring{A}$ to 2.4$\mathring{A}$ and in this section it was evident that the (101) peak for AlN (non-Centrosymmetric) and the (021) peak for B_4C was overpowered by the Al (111) peak because their d-spacing values are in proximity to each other and Al has a greater volume fraction compared to the volume fraction of B_4C. Also one of the

expected by-products of the cryomilling process is Iron Aluminum ($FeAl_6$). The peaks for this compound were visible and four $FeAl_6$ peaks were identified according to the JCPDS for non-centrosymmetric $FeAl_6$. One unidentified peak remained at 2.2665$\mathring{A}$ and was subsequently identified as an Aluminum Carbide (Al_4C_3) (107) peak also shown in Figure 2.7.

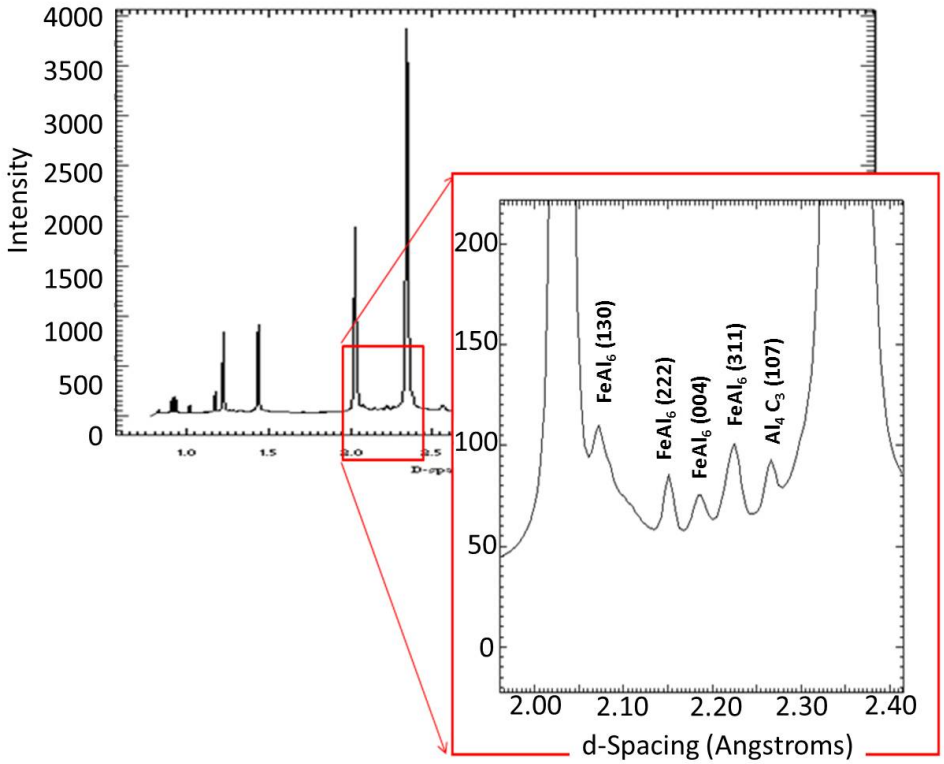

Figure 2.7: Zoomed in view of the lineout plot of the unloaded MMC sample at room temperature from 2.0$\mathring{A}$ to 2.5$\mathring{A}$

Figure 2.8 analyzes the lineout plot from d-spacing 2.5$\mathring{A}$ to 3$\mathring{A}$. Two additional $FeAl_6$ peaks were identified in this plot, further justifying the $FeAl_6$ found in Figure 2.7 previously. An AlN (100) peak (non-Centrosymmetric) was identified as well in this d-

spacing range. Furthermore, an Aluminum Carbide (Al_4C_3) (101) peak was also identified in this plot.

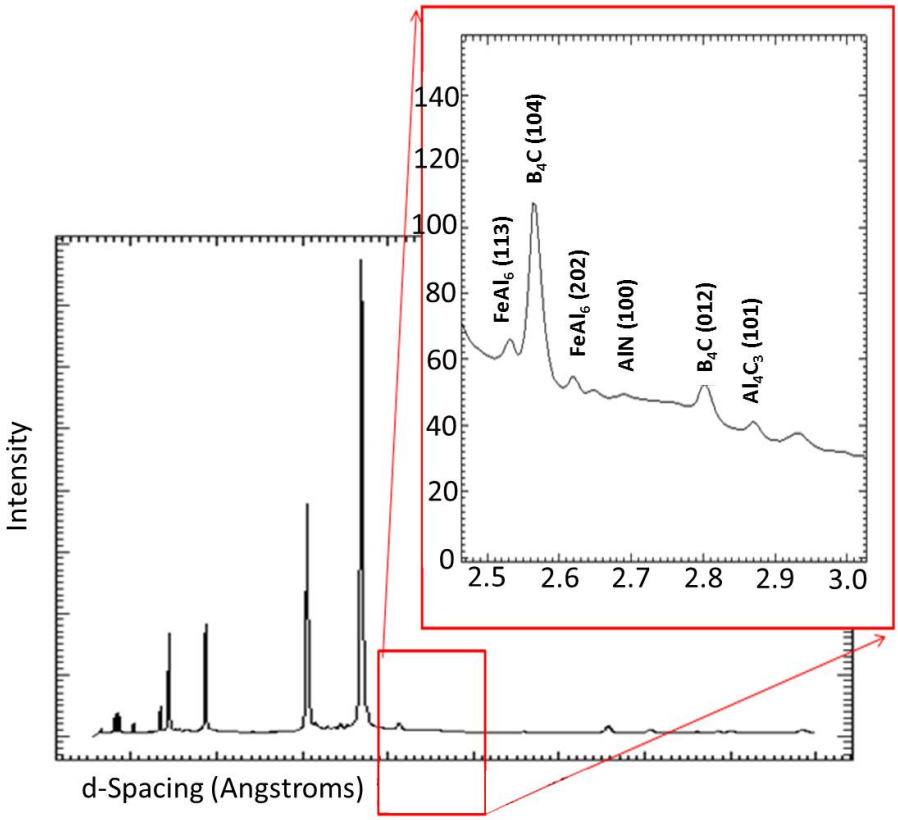

Figure 2.8: Zoomed in view of the lineout plot of the unloaded MMC sample at room temperature from 2.5$\mathring{A}$ to 3.0 $\mathring{A}$

Figure 2.9 (b) analyzes the lineout plot from d-spacing 4.5$\mathring{A}$ to 5$\mathring{A}$. This portion of the line out plot contained two peaks which were identified as the (101) peak for B_4C and the (110) peak for $FeAl_6$. The entire phase identification analysis revealed additional compounds in the MMC, such as $FeAl_6$, AlN, and Al_4C_3, all by-products of the cryomilling process. These peaks could have not been easily assessed if the experiment was done

under standard microscopy or lab-based XRD measurements due to their insignificant volume fractions compared to the main compounds such as Al and B_4C.

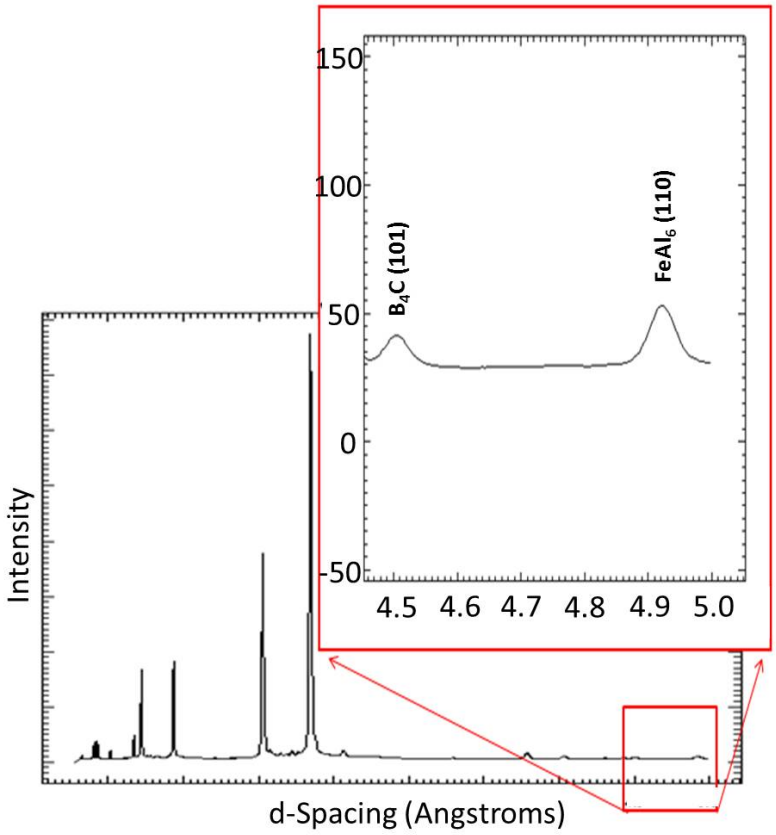

Figure 2.9: Zoomed in view of the lineout plot of the unloaded MMC sample at room temperature from $4.5\mathring{A}$ to $5.0\mathring{A}$

In a typical lineout plot obtained by XRD the intensity of the peaks will depend on factors such as the X-ray energy in addition to the volume percentage of the particular material. Therefore the use of the high energy synchrotron X-rays provided us with the capability of identifying peaks even for the compounds with small volume fractions. Obtaining all these peaks by synchrotron XRD can then help with the improvement of

the manufacturing process by relating this to the volume fractions of the compounds in-regards to the strength of the material. Taking this approach, future work will be to assess the volume fraction of these compounds using the intensities for various conditions of manufacturing to optimize the process while maintaining the mechanical properties.

2.2.2 Analyzing line widths to determine the grain size in MMC

In general, it is expected that the size of the nano Aluminum grains will grow as a function of thermo-mechanical loading. This growth can be inspected by comparing the line widths of the peaks in data collected at specific time intervals. Therefore after identifying peaks, the next task was to analyze the widths of the peaks which correspond to Al to draw a conclusion on the grain growth. Using the MATLAB based analysis program described in Appendix C, the Full Width Half Maximum (FWHM) was obtained for peaks with interest. The size of the nano Aluminum grains were estimated using Scherrer's Equation[47] as shown in Equation 2.5 where the FWHM was utilized as shown by the red lines in Figure 2.10. More specifically, according to the relationship, it is expected that the FWHM will decrease as a function of increased thermo mechanical loading.

$$\Gamma = \frac{K\lambda}{\cos\theta < L >} \tag{2.5}$$

Where K is 0.9 for spherical particles,

λ is the wavelength (nanometers),

θ is the diffraction angle (radians),

$< L >$ is the grain size (nanometers),

and Γ is the Full Width Half Max (radians).

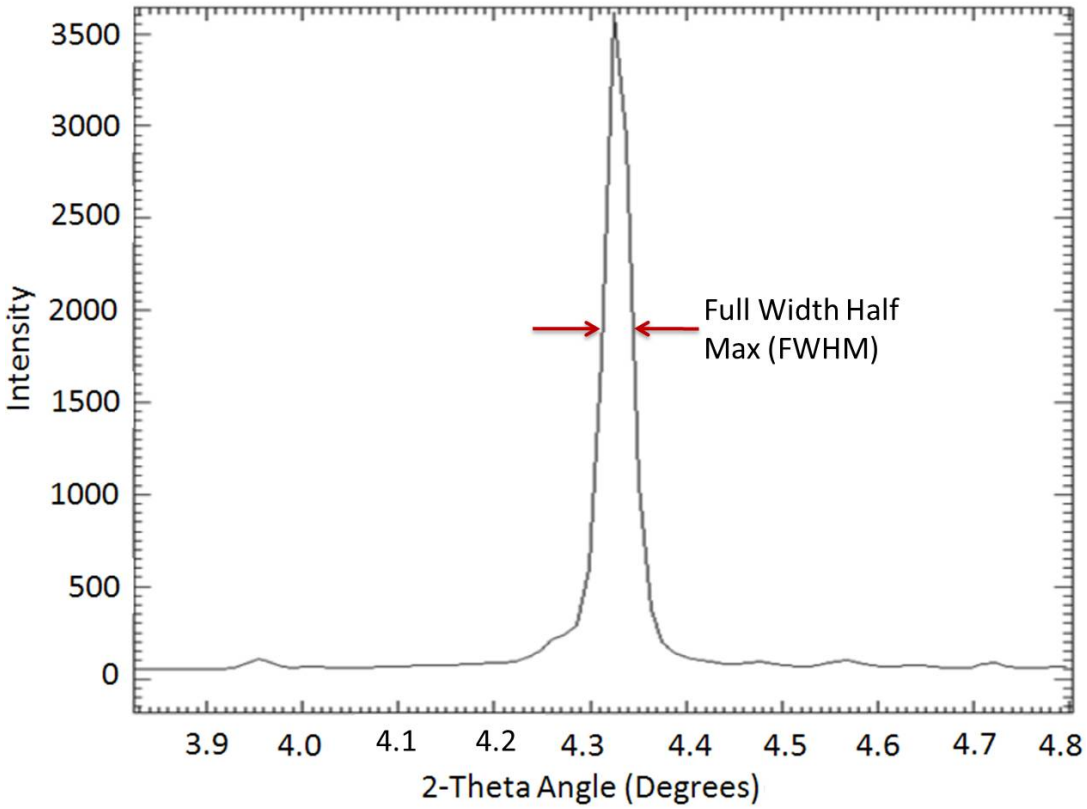

Figure 2.10: Intensity (counts) vs. 2-Theta Angle (Degrees) line out plot with FWHM identified in red

The FWHM value obtained from the analysis, initially in pixels, was converted to radians using the diffraction angle (2θ), the radius (r), and the sample-to-detector distance (z) as shown in Figure 2.11.

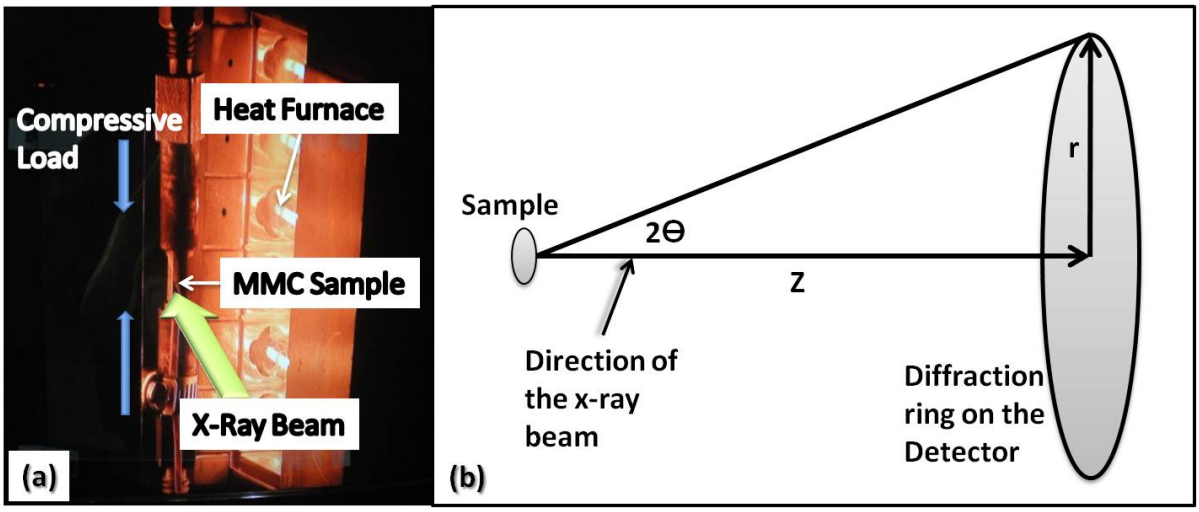

Figure 2.11: (a) Experiment setup of the MMC study (b) Schematic of the diffraction setup to analyze the grain size for MMC

From trigonometry,

$$\tan(2\theta) = \frac{r}{z} \tag{2.6}$$

Where θ is the diffraction angle (radians), r is the radius of the ring (mm), and z is the sample-to-detector distance (mm). Then taking the derivative and simplifying further,

$$d(2\theta) = \frac{dr}{z}.\cos^2(2\theta) \tag{2.7}$$

This value of $d(2\theta)$, which equals to the FWHM (radians), was substituted into Scherrer's Equation to determine the particle size $< L >$ (nanometers) at given time intervals.

Analysis on the 24 hour cryomilled powder revealed a nano Aluminum grain size of approximately 22 nm. Considering there is a distribution of grain sizes present, this value is similar to the expected 30 nm or lesser value visualized through TEM studies [45]. The grain-growth trend from a specimen which was under a thermo-mechanical load of 50MPa at 200^oC is presented in Figure 2.12.

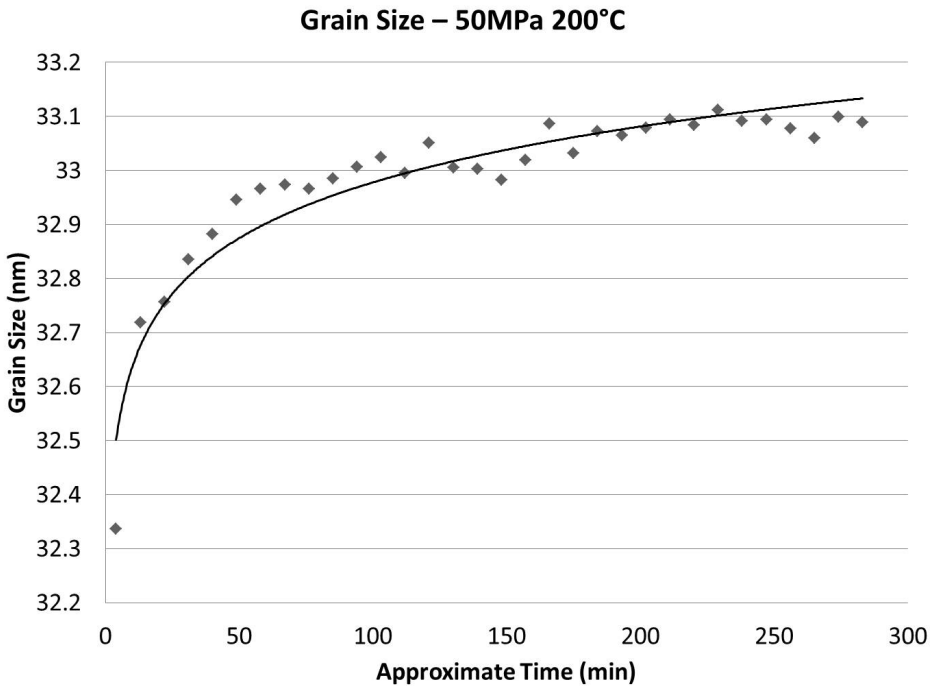

Figure 2.12: Grain Size (nm) vs. Approximate Time (min) for a sample under thermo-mechanical loading of 50MPa at 200^oC.

This work proved how synchrotron studies can successfully track and monitor growth of grains in MMC. The effects of mechanical loading on the FWHM at temperature can be be monitored as a function of time. Future work will be directed toward isolating the effects of instrumental and micro-strain broadening to determine more accurate grain size

measurements. Using this method it will be possible to accurately predict the optimum forging process time to have the optimum material properties.

2.3 Use of synchrotron X-ray diffraction on Thermal Barrier Coatings

High energy synchrotron X-ray transmission technique has proved itself as one of the most prominent methods to conduct a strain study for materials [48, 49, 50]. Since the beginning of the last century, numerous attempts have been made to correlate microstructural properties, such as texture and internal stress, to macroscopic behavior in polycrystalline materials. This is particularly significant for coatings grown by physical-vapor deposition (PVD) that often have high levels of texture and internal (residual) stress due to the inherently non-equilibrium nature of the deposition process [20]. Ex-situ XRD analysis has been successfully used on thermal barrier coatings to determine the strain in its layers, especially within the thermally grown oxide (TGO) layer [20, 21, 25, 27, 28, 29].

Strain measurement using synchrotron XRD is based on the distortion of the diffraction rings with applied loads on the sample. The diffraction ring for a compressed material changes its diameter with the applied stress and the strain related to this stress can be calculated as the result of a ratio of the change in d-spacing to the original d-spacing of an unstrained lattice, thereby yielding the strain information. The inter-planar spacing of the lattice, therefore acts as an internal strain gage [39]. For any diffraction ring, the

diameter is related to the sample-to-detector distance and the incident angle as illustrated in the previous equation 2.6. That equation can be rearranged as,

$$\theta = \frac{1}{2}\arctan(\frac{D}{2z}) \tag{2.8}$$

Where θ is the diffraction angle (radians)

D is the diameter of the ring (mm)

and z is the sample-to-detector distance (mm)

Combining this equation with Bragg's law,

$$d = \frac{\lambda}{2\sin(\frac{1}{2}\arctan(\frac{D}{2z}))} \tag{2.9}$$

Where d is the inter-planar distance

λ is the wavelength of the beam ($\mathring{A}$)

D is the diameter of the ring (mm)

and z is the sample-to-detector distance (mm)

For high energy X-rays such as those produced by the synchrotron, the diffraction angle is considered to be very small. Therefore the above equation can be simplified further as follows

$$d \approx \frac{\lambda z}{D} \tag{2.10}$$

The strain in a material would be the ratio of the change of the inter-planar distance to the original inter-planar distance. Using this information and the relationship between the inter-planar distance and the diameter of the diffraction ring which is inversely proportional the following relationship can be formulated

$$\varepsilon = \frac{d - d_0}{d_0} \approx \frac{D_0 - D}{D_0} \tag{2.11}$$

where ε is the strain in the lattice plane,

d is the new interplanar distance ($\mathring{A}$),

d_0 is the original interplaner distance ($\mathring{A}$),

D is the new diameter of the ring (mm) and

D_0 is the original diameter of the ring (mm).

2.3.1 Peak identification using synchrotron XRD data for Thermal Barrier Coatings

The complexity of peak identification for multi-material systems, in which the different atomic planes of various materials appear in the XRD spectrum, motivates the need to systematically identify the specific planes for which the characteristic peaks are easily discerned and can then be effectively monitored for strain in an in-situ context. Overlapping and low intensity peaks make the identification of suitable peaks challenging. In this section, the specific peaks that meet the criteria for effective strain measurement are

identified to complement the information from the relatively few synchrotron studies in this area. A step by step approach will be discussed on identifying the peaks for analysis in a TBC system which will form the basis of the in-situ studies detailed in Chapter 3.

The first step is to take data points from the layers in the TBC system. Figure 2.13 gives the reader an idea of the scanning of the layers by the synchrotron X-ray beam. The experimental setup will be elaborated in Chapter 3.

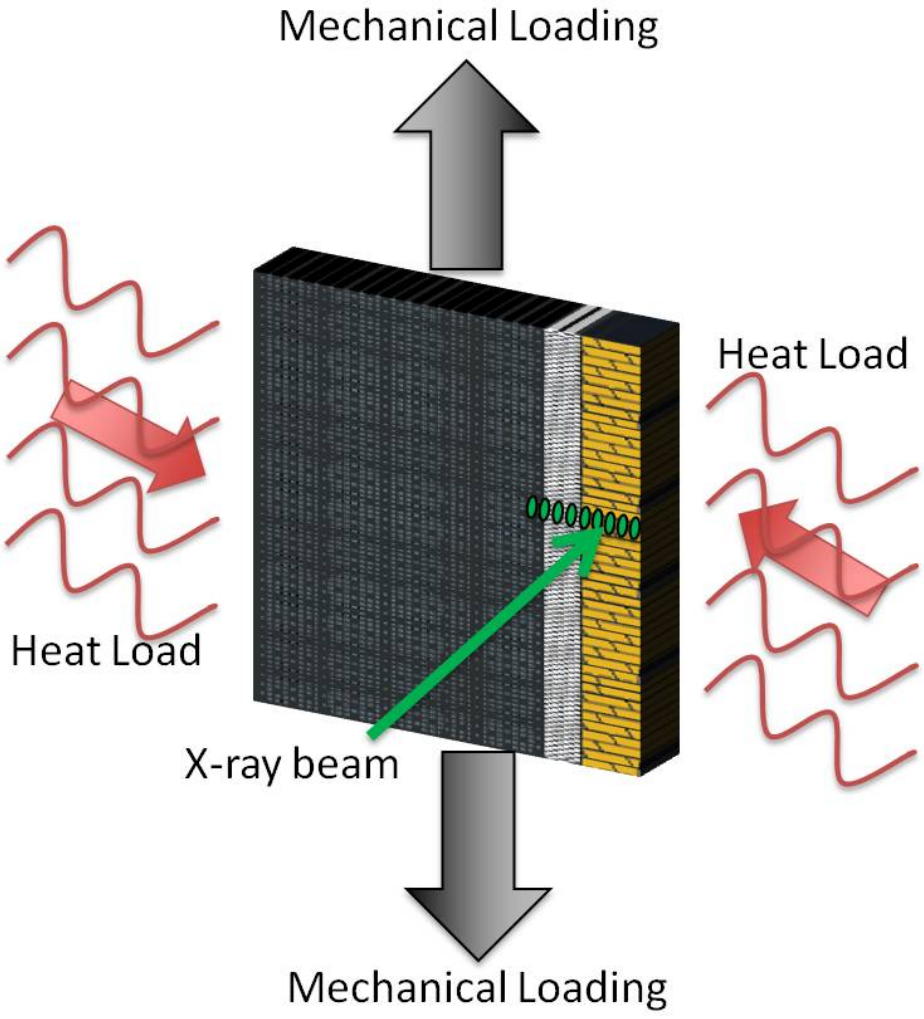

Figure 2.13: Scan of the layers by the X-ray beam

As discussed, the three main layers of interest in the TBC system are the top coat which contains Zirconium Yttrium Oxide (ZrO_2+Y_2O_3), TGO layer which contains $\alpha - Al_2O_3$, and the bond coat which contains NiAl. For this section, a data set from the sample which was at room temperature under a low external stress (16 MPa) was taken into consideration.

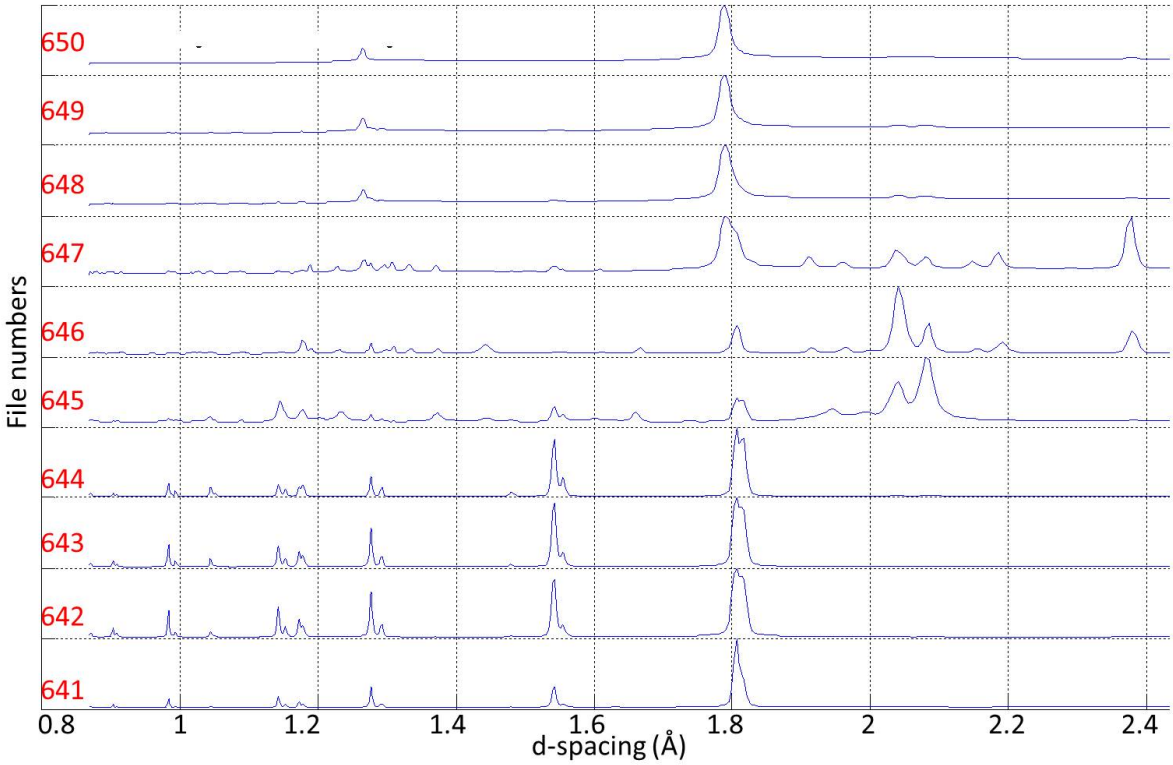

Figure 2.14: X-ray diffraction lineouts of the different layers at a certain time step before identification

The lineout plots from multiple data points taken across the TBC depth were created together as seen in Figure 2.14. Each of these file numbers (641-650) corresponds to

a depth spot in the TBC system as illustrated in Figure 2.13. The scanning typically starts with the top coat layer and moves through the layers towards the substrate. The complexity of an in-situ temperature measurement is contributed by the expansion of the materials which renders the data collection over the cycle a dynamic situation.

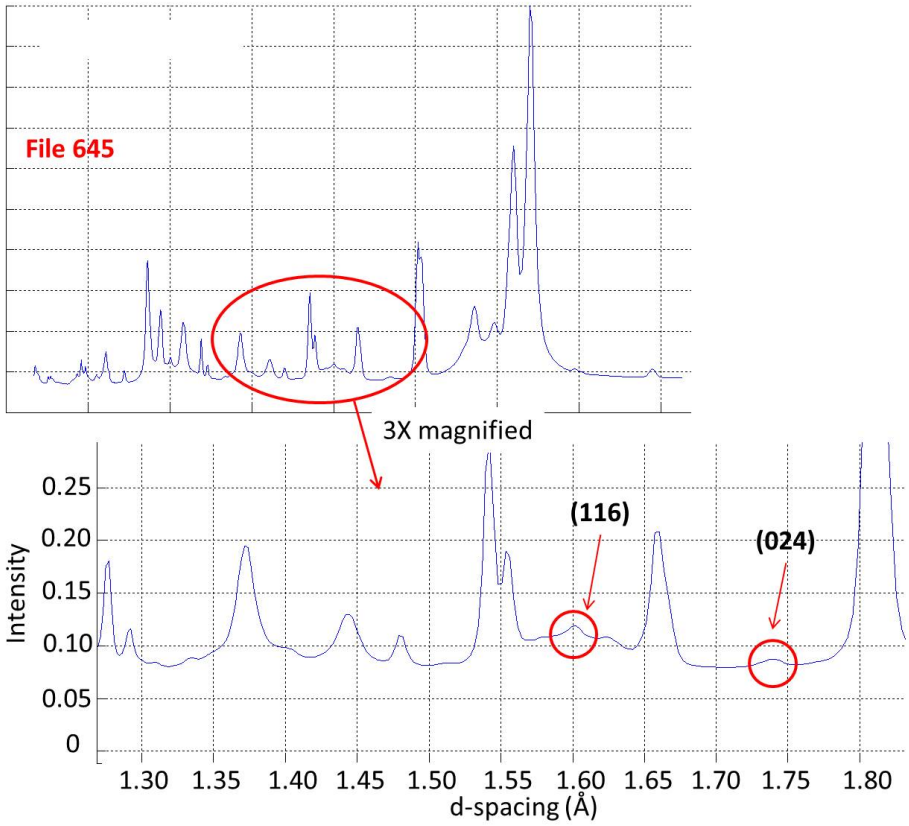

Figure 2.15: Lineout plot for the TGO layer

The next step would be to identify which lineout plot corresponds to the TGO layer. According to Table A.1 in the Appendix, for $\alpha - Al_2O_3$, the (116) peak corresponds to $1.6006\mathring{A}$ d-spacing value, (300) peak corresponds to $1.3733\mathring{A}$, and (024) peak corresponds to $1.7396\mathring{A}$. These three peaks are supposed to have a relative intensity of 2:1.5:1 respec-

tively. A zoomed in view shows two of these peaks, (116) and (024) according to their d-spacing and intensity compared to each other, in the file number 645 as illustrated in Figure 2.15.

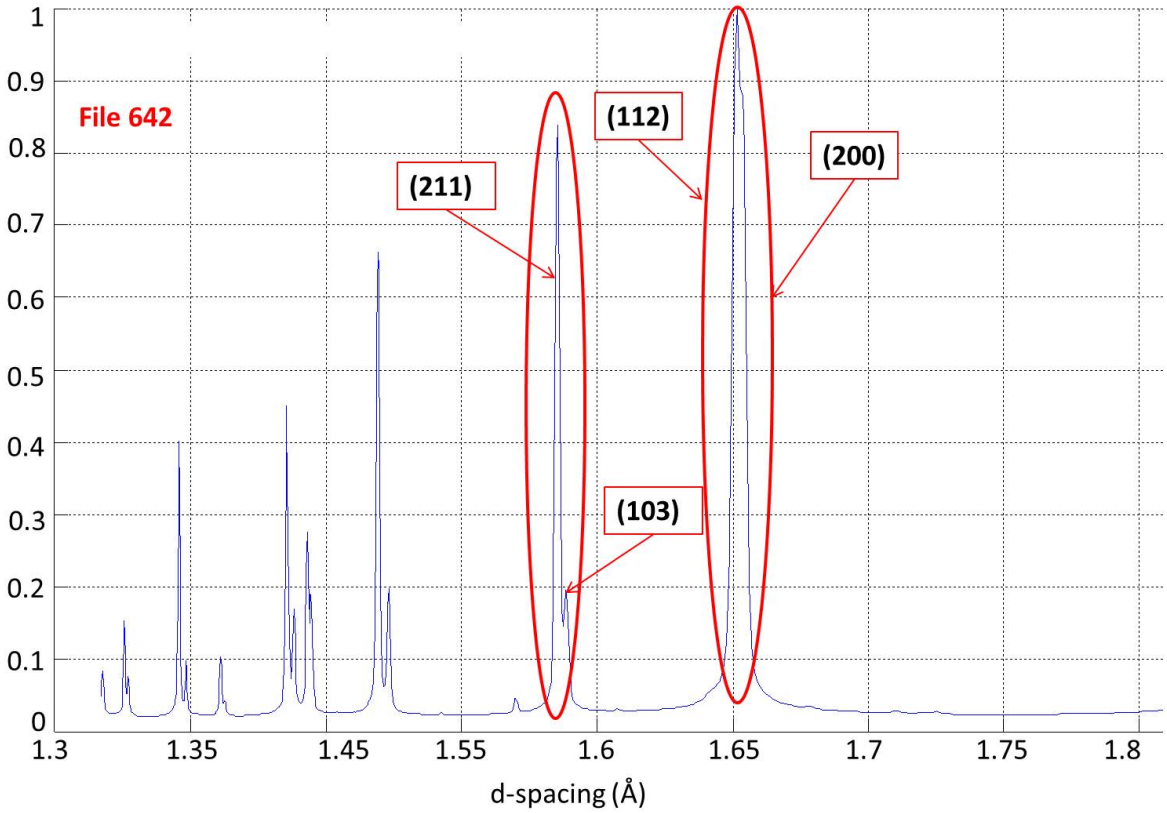

Figure 2.16: Lineout plot for the YSZ layer

Due to the width of the X-ray beam being larger than the TGO layer thickness, the scan which will capture the TGO layer will include the diffraction patters from the YSZ as well as the BC. If two different peaks from two materials have the same d-spacing, these will clearly overlap each other. In this case since the YSZ peaks have much higher

intensities, compared to TGO peak intensities, the TGO peaks may be masked by the YSZ peaks. Once the lineout plot for the TGO layer is identified, the neighboring lineout plots were confirmed to either belong to the YSZ or the bond coat.

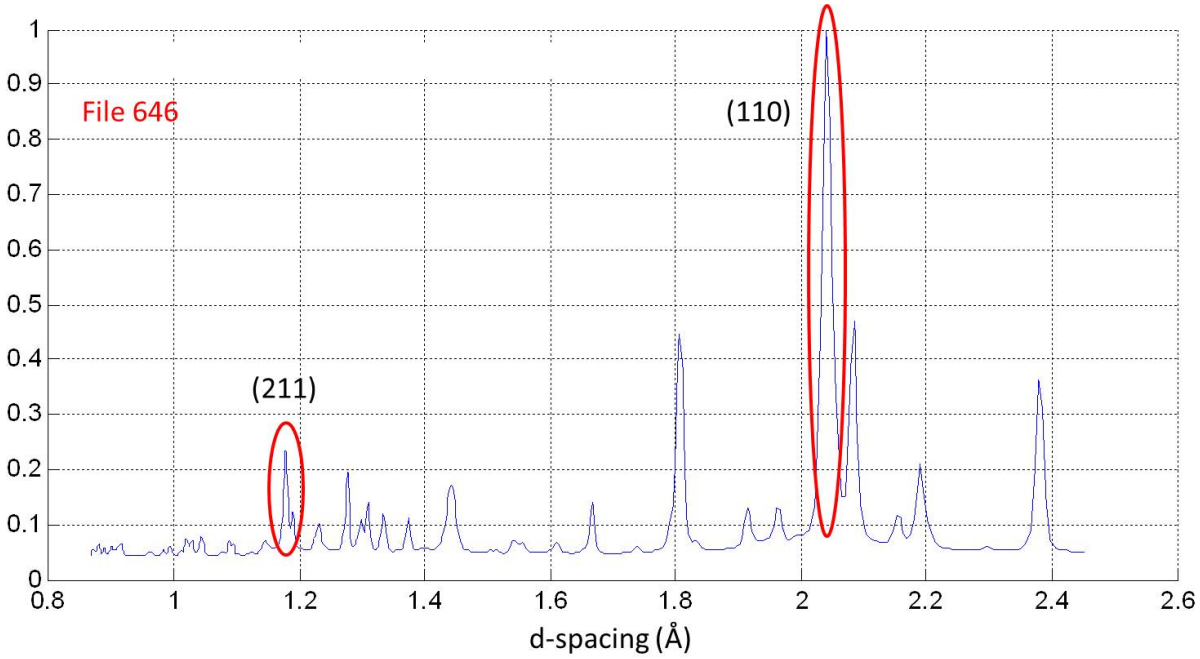

Figure 2.17: Lineout plot for the Bond coat layer

According to Table A.4 in the Appendix, for YSZ, peak (112) corresponds to 1.8149$\mathring{A}$, (200) corresponds to 1.8149$\mathring{A}$, (103) corresponds to 1.5491$\mathring{A}$, and (211) corresponds to 1.5461$\mathring{A}$ and they have an intensity ratio of 3.5:2:1:2.5 respectively. Out of these four peaks, (112) and (200) appear to be double peaks where the two peaks are attached to each other since their d-spacing values are close to each other. Peaks (103) and (211) appear to be double peaks due to the same reason. A zoomed in view shows these double peaks in the file number 642 as illustrated in Figure 2.16.

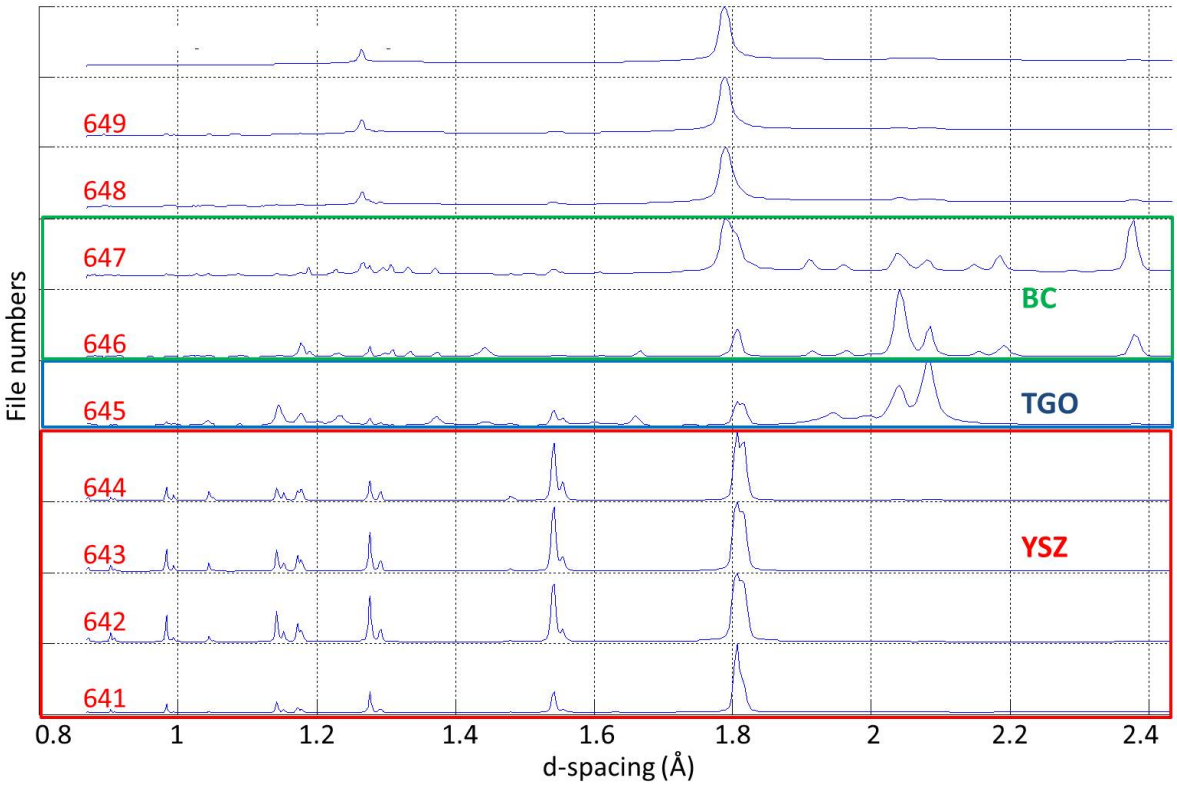

Figure 2.18: X-ray diffraction lineouts of the different layers at a certain time step after identification

According to Table A.5 in the Appendix, for the bond coat, peak (110) corresponds to 2.0393$\mathring{A}$, (211) corresponds to 1.1774$\mathring{A}$, and (100) corresponds to 2.884$\mathring{A}$. The intensity of these peaks take the ratio 5.75:1.2:1 respectively. A zoomed in view shows two of these peaks in the file number 646 as illustrated in Figure 2.17. Figure 2.18 has all the layers identified and these will be used in the process of analyzing strain measurements.

2.3.2 Analyzing peak positions to determine the strain in TBC

With the presence of strain, the diffraction rings will change their shape from perfect concentric circles to a shape assumed to be an ellipse [49]. This means each peak on the lineout plot will shift along the whole azimuth. The lineout plots that have been presented, indicate an average of the shifts over the complete azimuth. Therefore in order to determine the strains, the selected diffraction ring must be integrated around the azimuth resulting in a final bi-strain plot for the particular ring.

Here, the file 645 from the previous section, would be considered since that was identified to be the TGO layer. As illustrated in Figure 2.15, file 645 has peaks of planes (116) and (024) evident for the TGO material and both these rings were integrated for strain analysis to validate each other. First, the peak has to be defined and since the peak (116) needs to be analyzed, corresponding data such as the lattice parameters and the Miller indices (hkl) values has to be considered.

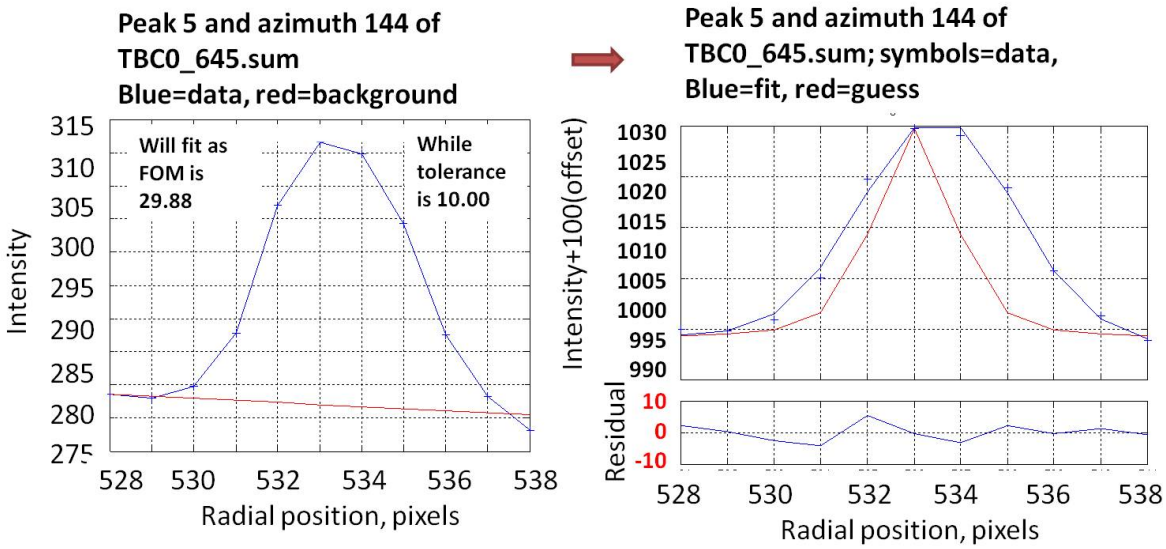

Figure 2.19: Fitting of the $\alpha - Al_2O_3$ (116) peak at a particular azimuth value

The fitting of the peaks is the next stage of the analysis. According to the lattice parameters and the Miller indices (hkl) values, the particular peak will go through a fitting process as shown in Figure 2.19. This fitting process will be carried out along the entire azimuth.

The bi-strain is obtained by considering the shift of the vertices of the peaks along the azimuth as illustrated in Figure 2.20 for the peak (116). The axial strain on the TGO layer was found to be -0.004703 indicating a compressive value. This strain found using the (116) peak was then verified with (024) peak. Figure 2.21 illustrates the bi-strain profile obtained from peak (024) and this strain value of -0.004262 agrees with the result from the (116) peak with a 9% error which is sufficient for the verification process.

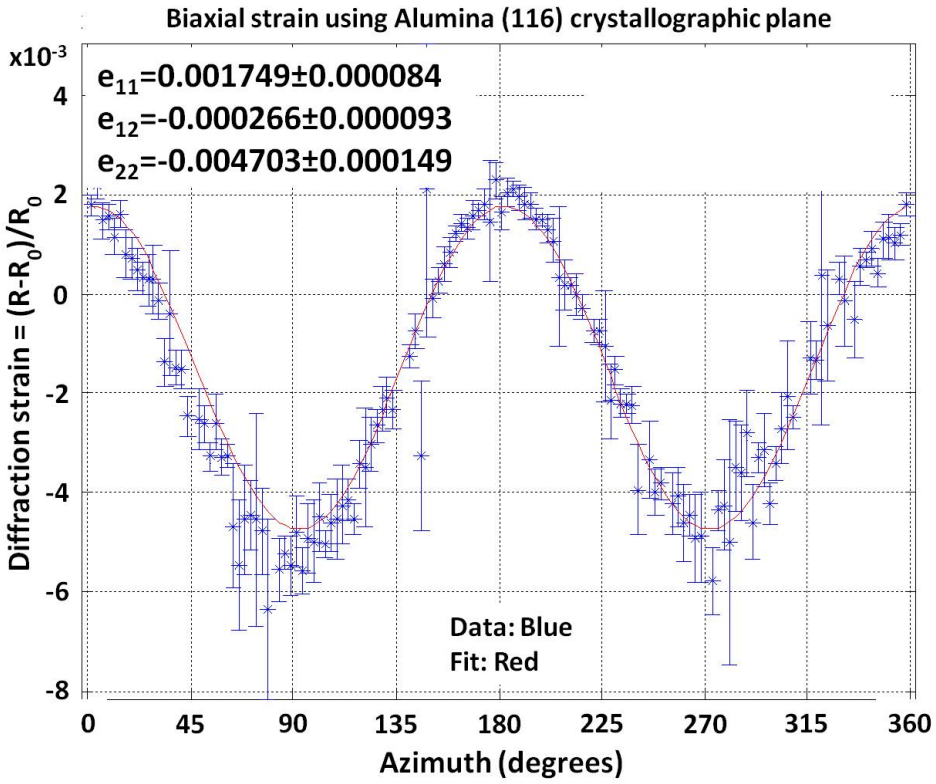

Figure 2.20: Bi-strain profile obtained for the TGO layer using peak (116)

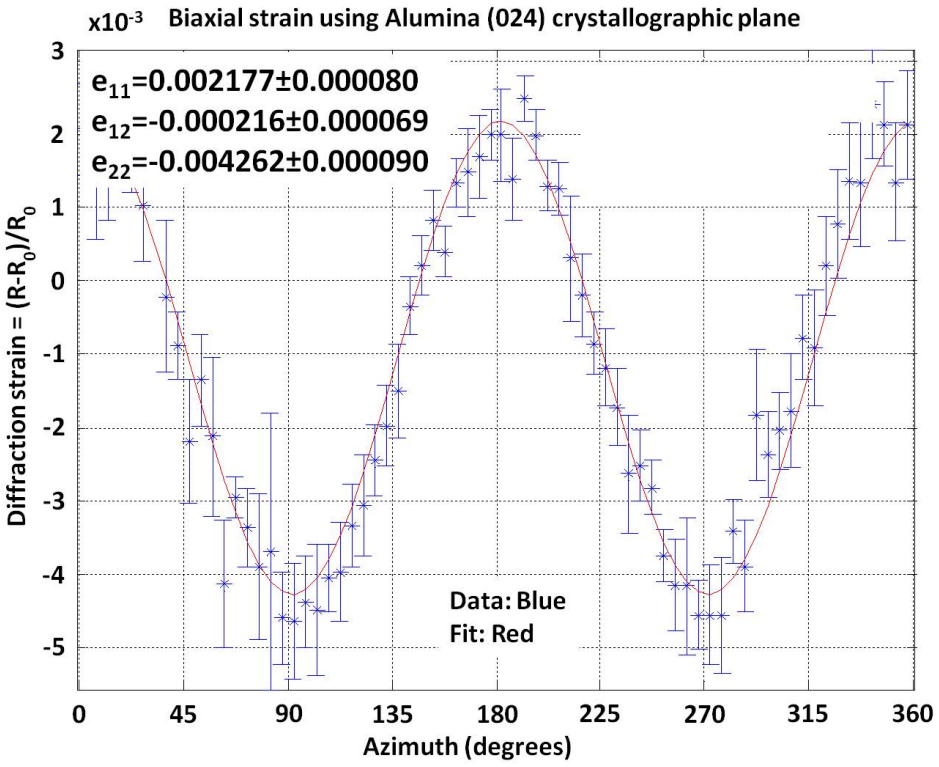

Figure 2.21: Bi-strain profile obtained for the TGO layer using peak (024)

The diffraction information included in the appendices represents data at ambient temperature. At high temperatures, the d-spacing values for the peaks will require adjustment. Hence a correction was applied since the peaks are shifted with temperature as illustrated in Figure 2.22.

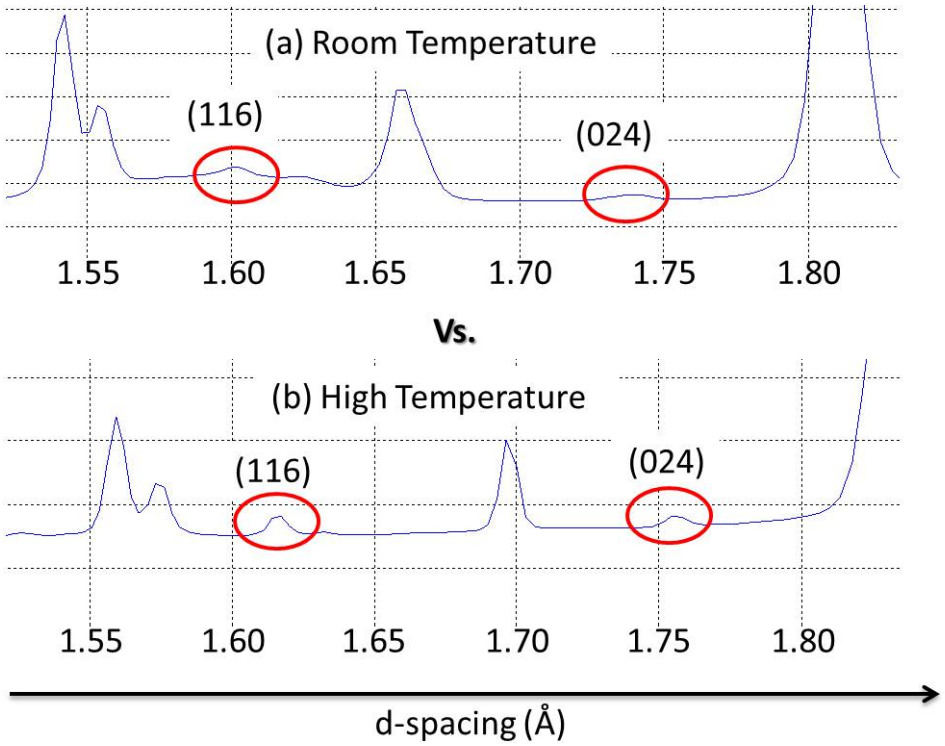

Figure 2.22: (a) Room temperature lineout vs. (b) High temperature lineout

At high temperature the peaks have shifted right from their original position. To compensate for this, the fitting parameter was changed in the analysis according to the Equation 2.12.

$$a^* = a(1 + \alpha T) \tag{2.12}$$

Where a^* is the fitting parameter value at that temperature

a is the lattice parameter value needed for the fitting process at room temperature

α is the thermal expansion coefficient for the particular material

and T is the temperature.

These bi-strain values obtained for each of the layers of the TBC system at different temperatures along the thermal cycle while under varying mechanical loading will be presented in the next chapter. The effect of the thermo-mechanical loading on the life of the TBC coating will be analyzed and discussed.

CHAPTER 3
EFFECT OF THERMO-MECHANICAL LOADING ON THE TBC STRAIN USING XRD MEASUREMENTS

3.1 Objective

Numerous experimental efforts aimed at establishing strains within the TBC system reiterate the significance of quantitative strain determination [14, 51, 52, 40] and its role in life prediction of the coatings. Most of these studies were performed as ex-situ furnace tests to establish the effect of the thermal cycling on the coating strains. In parallel research on turbine blade fatigue, the mechanical loads representing centrifugal forces have been considered with a focus on the resulting coating effects on the blade life model [31, 32, 33]. In our research, a novel approach was taken to monitor the strain evolution under simultaneous thermal and mechanical conditions by combining the experimental setup with high energy X-rays at a synchrotron facility. The goal of enhancing experimental conditions to closely simulate the operational conditions of the turbine blades, by considering the mechanical loading, is to capture the effects on the strain within the TGO and therefore the overall life of the coating. Generally, a complete thermal cycle experienced by jet engine turbine blades can be represented by a start at room temperature with a ramp up to approximately 1120^oC, a subsequent hold at constant high temperature followed by a ramp down. The mechanical load representing the centrifugal forces may be simulated with a constant stress applied to the sample during this cycle. Kitazawa et al. [34] conducted studies to evaluate the damage of a

TBC system under in-phase thermo-mechanical tests where failure was observed using optical microscopy. In their research, an external uniaxial applied stress of 60MPa was used and the damage evaluated.

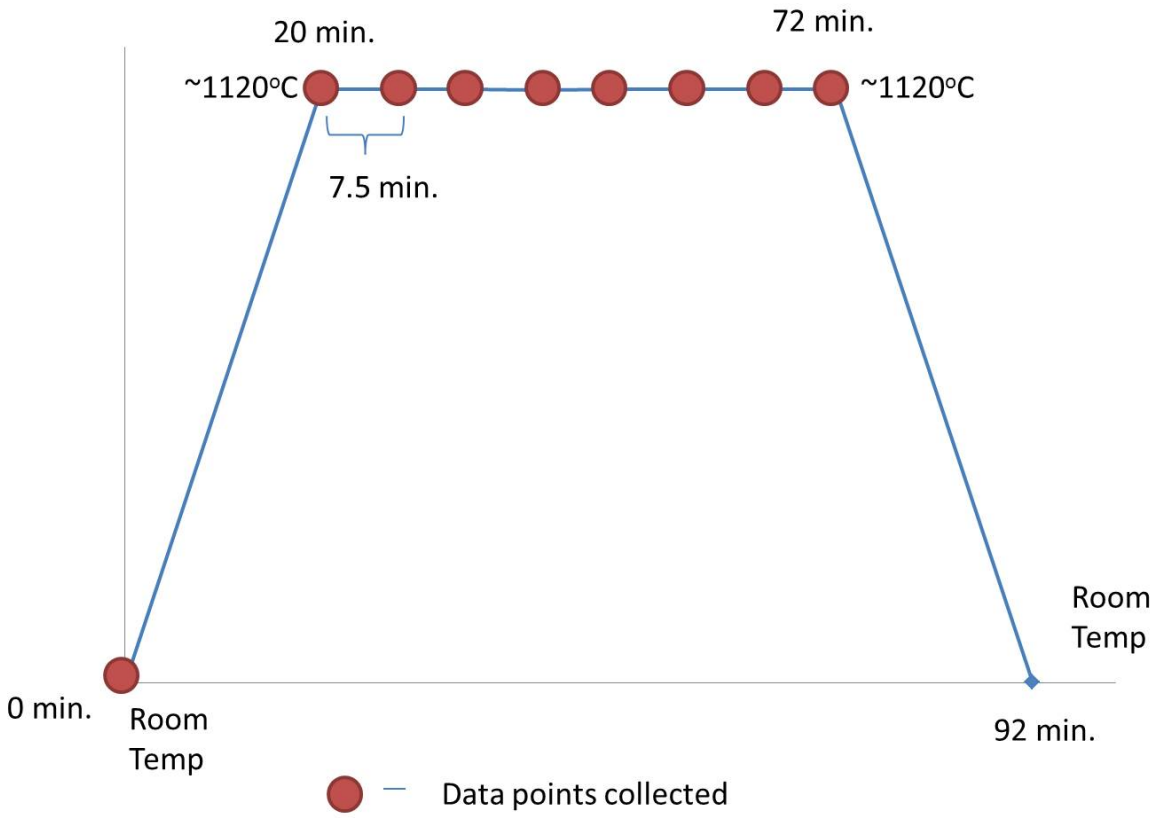

Figure 3.1: Thermal cycle used in the experiment

In thermal mechanical fatigue tests with controlled thermal gradients (TGMF conducted by Bartsch et al. [35], an external mechanical loading up to 100MPa was used. This study identified a class of fatigue cracks that occured only in TGMF tests and not in isothermal low cycle fatigue or thermal fatigue. Ray et al. [53] studied the evaluation

of TBC life using accelerated creep tests and they used an external mechanical loading of 70MPa.

In our research, an initial external applied stress of 16MPa corresponds to the least load needed for the sample to be held properly in the loading cell. Additional loads corresponding to stresses of 32MPa and a maximum of 64MPa were applied for comparison purposes with previous thermo-mechanical studies. For the experiments conducted in this work, the thermo-mechanical cycle was recreated with a starting room temperature, ramp up for 20 minutes to the high temperature in the range of 1120^oC and a constant hold at this temperature for 52 minutes while in-situ XRD measurements were taken about every 7.5 minutes over the depth of the multi-layered TBC as illustrated in the Figure 3.1. Constant stress values were maintained during the experiments at the 3 different values to determine the effects of increasing applied stress on the strain evolution.

3.2 XRD Experimental Setup

The samples used in the experiments performed for this work were Electron Beam Physical Vapor Deposition (EB-PVD) coated on a nickel-based super-alloy substrate. EB-PVD is based on a method where a target anode reacts with an electron beam produced by charged tungsten inside a vacuum. This reaction produces vapor of the target and this vapor is solidified on top of the surface to create a coating [54]. The TBC system has

a top coat which is Yttria-Stabilized Zirconia (YSZ) and takes the form of a columnar structure while the platinum-modified nickel-aluminide (PtNiAl) bond coat provides a good bond between the coating and the substrate. In the EB-PVD process and also during a thermal cycle, oxygen (O_2) from the environment penetrates through the columnar structure of the top coat and reacts with the Aluminum (Al) in the bond coat to oxidize and produce the thermally grown oxide layer that forms and grows between these layers. In Chapter 1, Figure 1.1 illustrates these various layers of the TBC system discussed here.

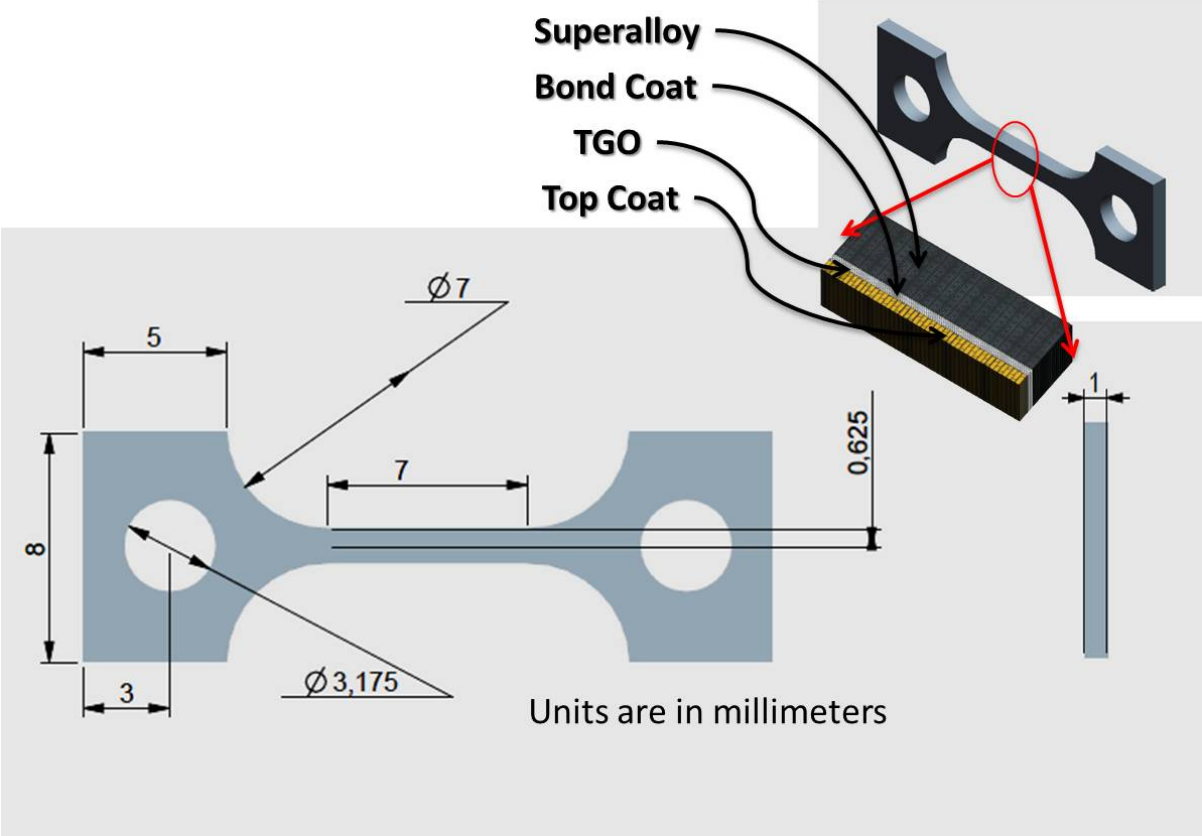

Figure 3.2: Scematic of the sample used in this research [3]

For this research, samples specimens were prepared from one inch diameter CMSX-4 Ni-base super-alloy discs with a platinum-modified nickel-aluminide bond coat (50 μm) and 7 weight percent Yttria-stabilized zirconia (7YSZ) EB-PVD TBC (125 μm).

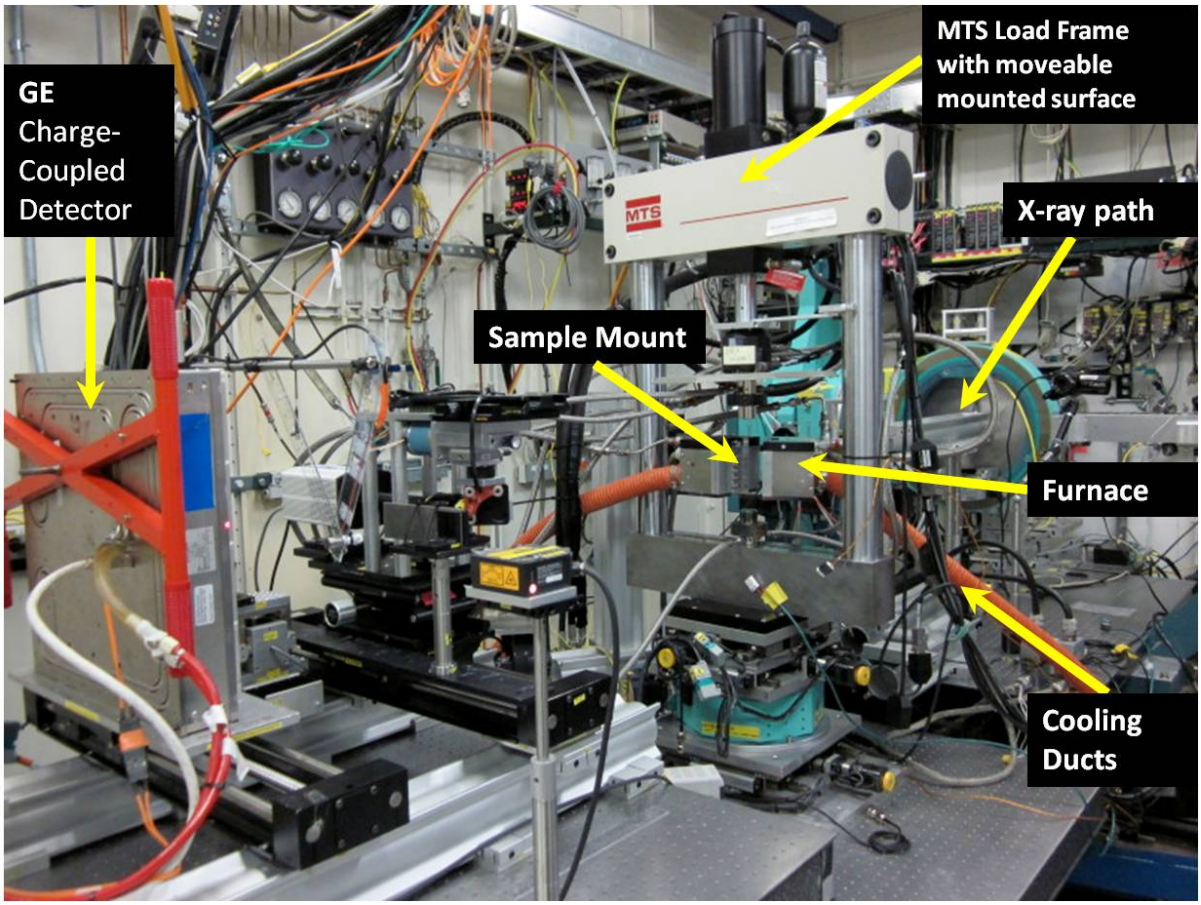

Figure 3.3: Experimental setup at 1-ID [3] sector at ANL

The test specimens were cut with a "FLOJET" Water Jet with an operational pressure of 40,000 psi using 100 HAD Garnet sand. The machine has a tolerance of 1/1000 inch and had a repeatability of 3/1000 inch. Sample specimens were machined to ASTM

standard E 8/E 8M [55, 3] . Figure 3.2 illustrates the sample prepared for this research with the dimensions.

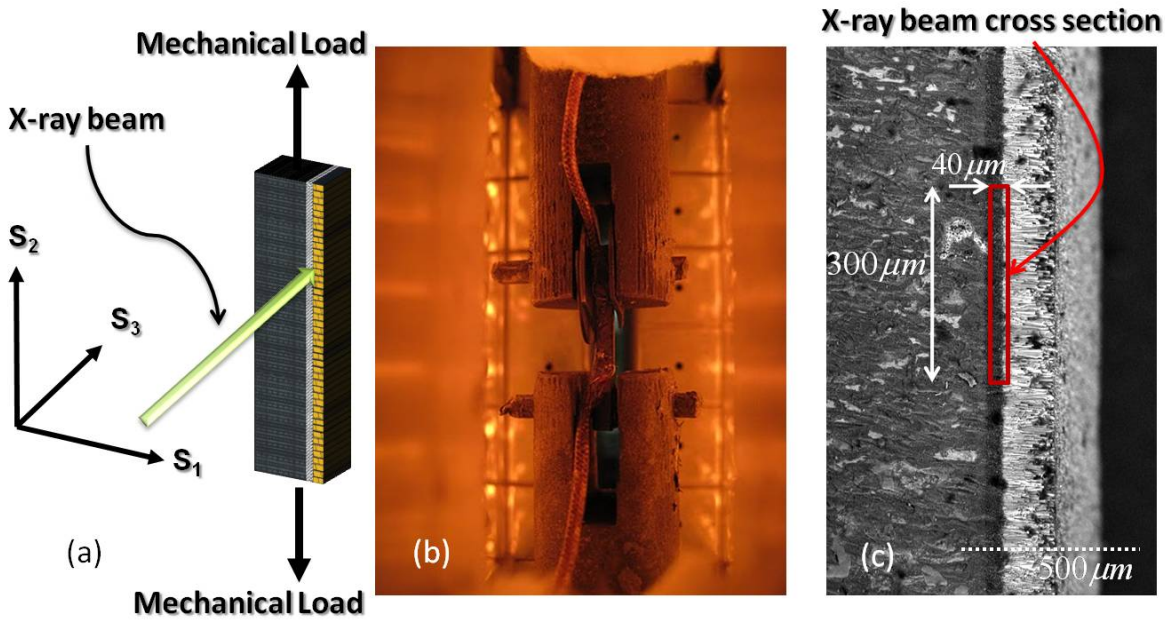

Figure 3.4: (a) Sample schematic with the coordinate system considered in the experiment [3]. (b) Sample mounted in the load frame while under thermo-mechanical loading [3]. (c) SEM image of the TBC coating with a representation of the $40\mu m$ by $300\mu m$ cross-section of the X-ray beam.

The experiments were performed at the 1-ID beam line at the Advanced Photon Source (APS) at Argonne National Laboratory. This beam line had the capability to produce high energy beams in the range of 100keV ideal for high resolution strain measurements in short data collection times. In our experiments, high energy X-rays of 86keV were used obtain depth-resolved data across the layers. Figure 3.3 illustrates the

experimental facility with an MTS (858 frame) load cell on an XYZ stage to obtain the needed orientation, an infra-red furnace to provide the thermal cycling and also a 2D XRD detector with a resolution of 2048 pixels x 2048 pixels, used to collect the data of the diffraction rings.

The sample was mounted as illustrated in Figure 3.4 (b) in the load frame using pins and the temperature monitored using thermocouples. Depth-resolved data was collected for applied stress values of 16MPa, 32MPa and 64MPa. Using the XYZ stage of the MTS machine, data could be collected for different depth values across the layers in the S_1 axis at a rate of 0.04mm per reading. The dimensions of the X-ray beam were $40\mu m$ by $300\mu m$ as illustrated in Figure 3.4 (c). Considering the co-ordinate system presented in Figure 3.4(a), the layers of the coating system are oriented along the S_1 axis on the Nickel super-alloy substrate and the path of the X-ray beam was along the S_3 axis.

For each time step in the thermal cycle as illustrated in Figure 3.1, approximately 10 data points were collected and this was repeated for all three (16MPa, 32MPa, and 64PMa) different loading conditions. The X-ray beam cross section as illustrated in Figure 3.4 (c) was adjusted to the edge of the YSZ layer and moved in the negative S_1 direction shown in Figure 3.4 (a) while data was collected across the layers. The diffraction patterns collected for all the layers in a cycle for each thermo-mechanical loading condition is shown in Figure 3.5. The XRD patterns were analyzed through a systematic procedure described in Section 2.3. As discussed, to be consistent with the studies by Kitazawa et al. [34] 64MPa was used as the maximum load for the study.

Using the XYZ stage of the MTS machine, data could be collected for different depth values across the layers in the S_1 axis at a rate of 0.04mm per reading.

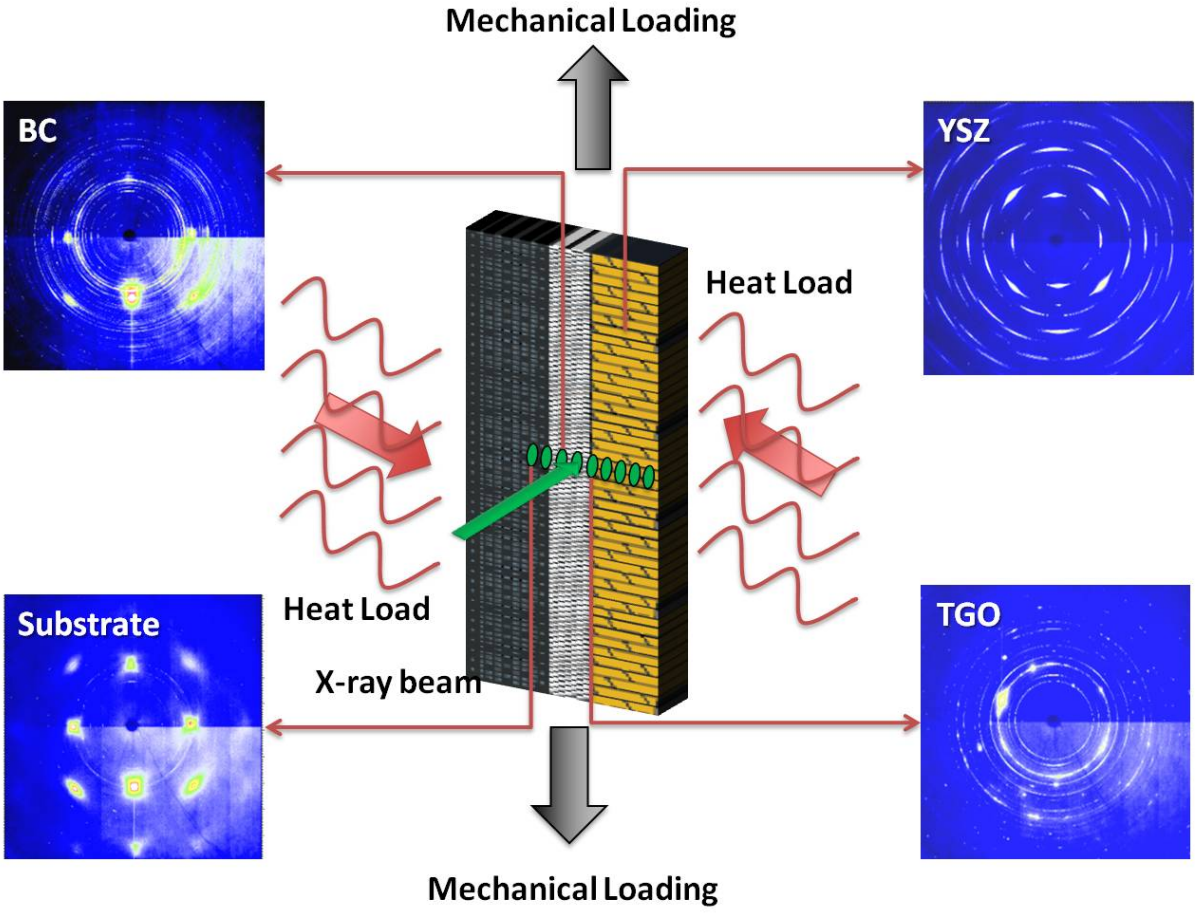

Figure 3.5: Example diffraction patterns obtained for different layers in the TBC sample

3.3 Results

The results from the analysis of the diffraction data collected in the thermo-mechanical experiments are presented here in terms of the i) strain evolution in the TGO layer as well as ii) depth profiles indicating the strain evolution across the layers of the TBC system. These results were obtained during the thermal cycle with different mechanical loadings. Contour plots of the strain evolution enable a visual representation of the changes in strain over the depth of the sample and are based on in-situ high resolution strain results.

3.3.1 TGO strains and the tensile region

After obtaining the TGO strain at any given time step, that strain can be converted to the stress and that could be related to a particular remaining life cycle fraction of the layer. The strain evolution based on the collected data during a thermal cycle provided in Figure 3.1 is presented here for the TGO layer. This analysis was done for all three different loading conditions and presented in Figure 3.6.

As it illustrates for low external stresses such as 16MPa and 32MPa, the strain was always in the compressive region. When the higher external stress of 64MPa was introduced, a tensile strain was observed in the ramp up position of the cycle. This tensile strain could have an effect on the failure of the TBC over several cycles and this will be

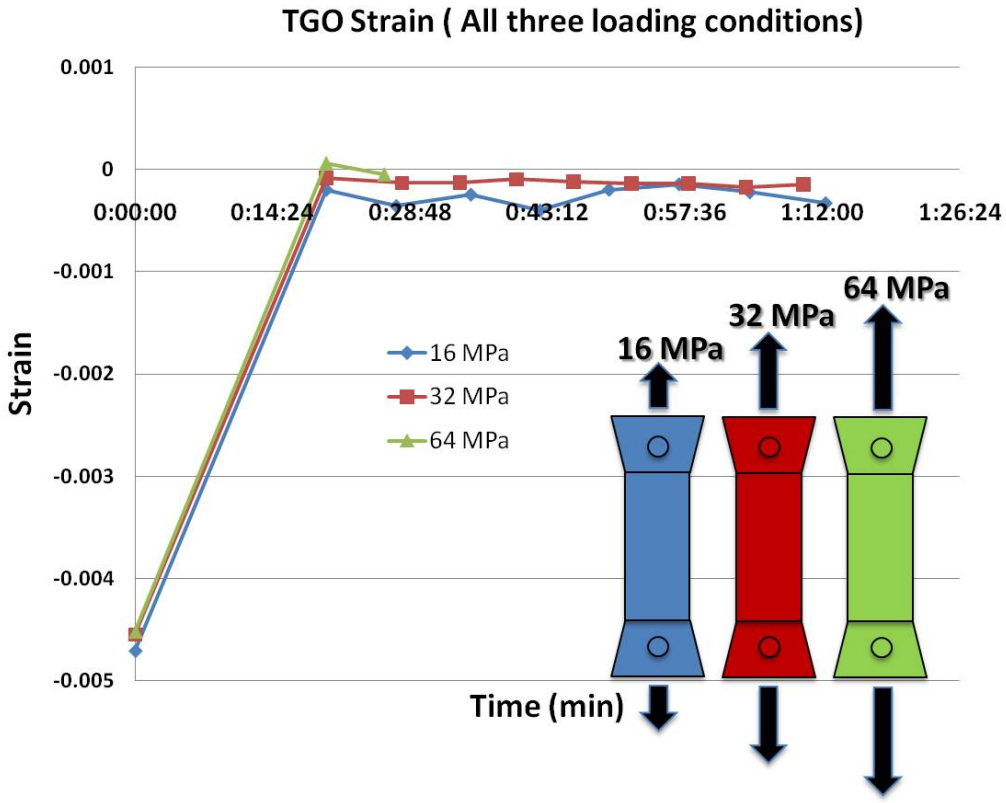

Figure 3.6: Strain evolution during a cycle for all three loading conditions.

discussed later in the chapter. This highlights the importance of considering the mechanical loading along with thermal load when analyzing the strain in the TGO layer. Results for the stress of 64MPa were limited to 3 data points due to failure of the retension pins.

3.3.2 Strain in the overall TBC system

This section presents the results obtained for the overall strain evolution in the various layers of the TBC system represented as graphs and contour plots. Figure 3.7 illustrates the stain profile for the various layers in the TBC at room temperature. While the TGO layer has the most compressive strain in the TBC system, no distinct changes in the strain profiles are observed with varying mechanical loading. Although mechanical loads at room temperature are not representative of actual operating conditions, this data is used for comparison with PSLS method for resolution improvement suggestions presented in Chapter 4. The effects of mechanical load will play an important part during the rest of the thermal cycle as will be discussed later in the Chapter.

Depth profiles at various stages during the cycle for the three mechanical loading conditions are presented as contour plots. An example plot illustrating the layer representation on a contour plot is shown in Figure 3.8. The significant part of the contour plot is the TGO layer.

Figure 3.9 represents the contour plots of the TBC system for the various loading conditions at room temperature.The YSZ and bond coat layers were in a tensile region in contrast to the high compressive strain the TGO layer was experiencing. The strain from the outer surface of the YSZ at low loads are observed to increase from low tensile values towards compressive values as it approaches the interface between the YSZ and the TGO.

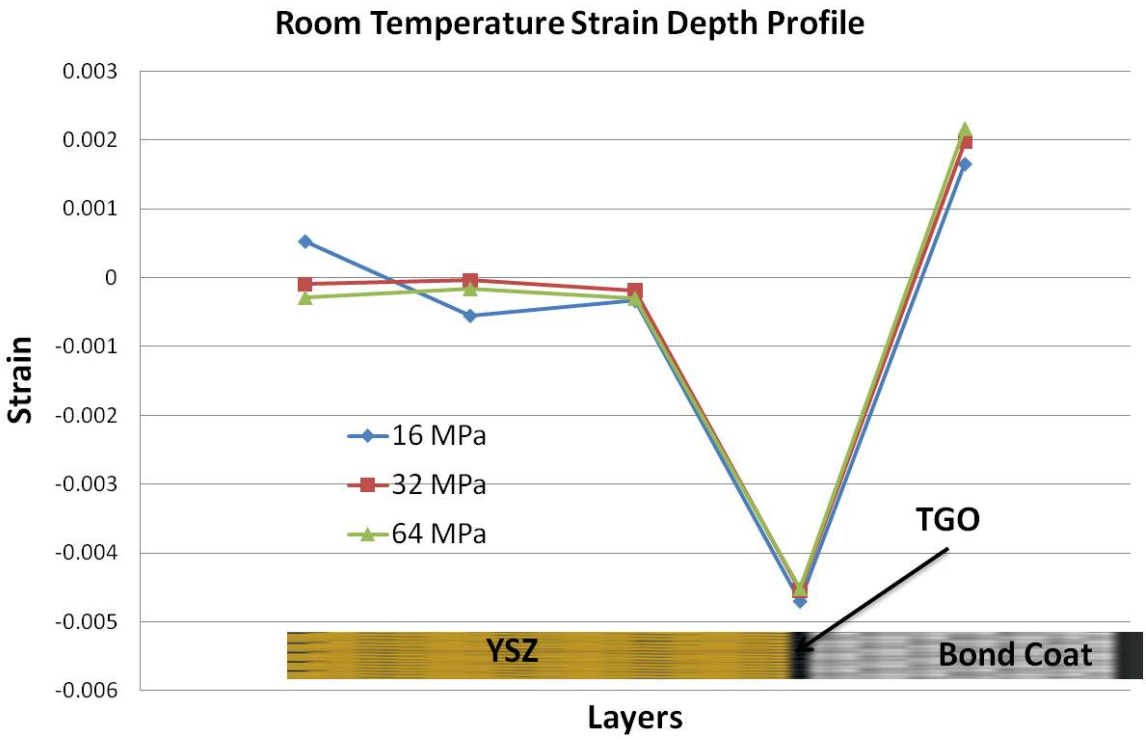

Figure 3.7: Depth profile of the strains during different cycles

This behavior has been presented in depth resolved studies for cycled specimens [29]. The variation of mechanical loads has a slight effect on the strains in the YSZ with less tensile strains were seen with the higher loads. There were no significant variations in strain in the TGO layer observed for all three applied loading conditions. The small variations are presented in Figure 3.10 from which it was observed that the strain was actually increasing towards less compressive values with increasing external mechanical loading.

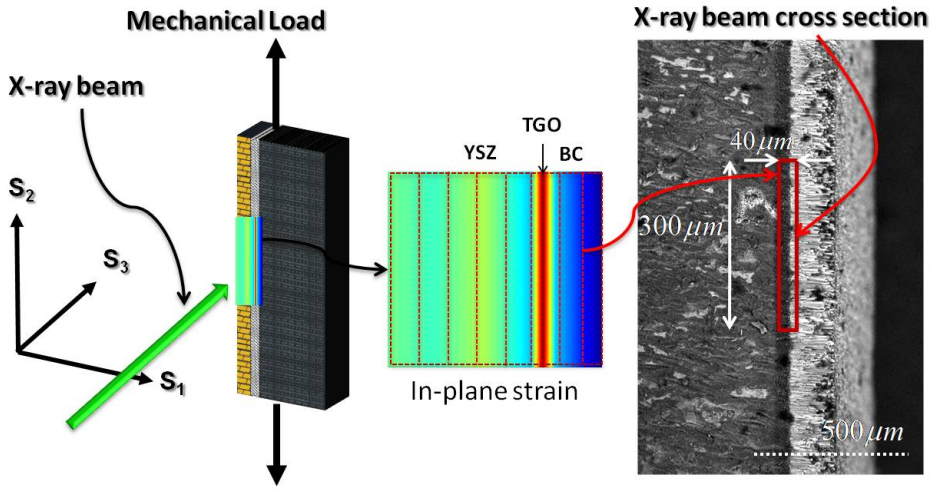

Figure 3.8: Contour plots used according to the depth of the layers (drawn to approximate scale)

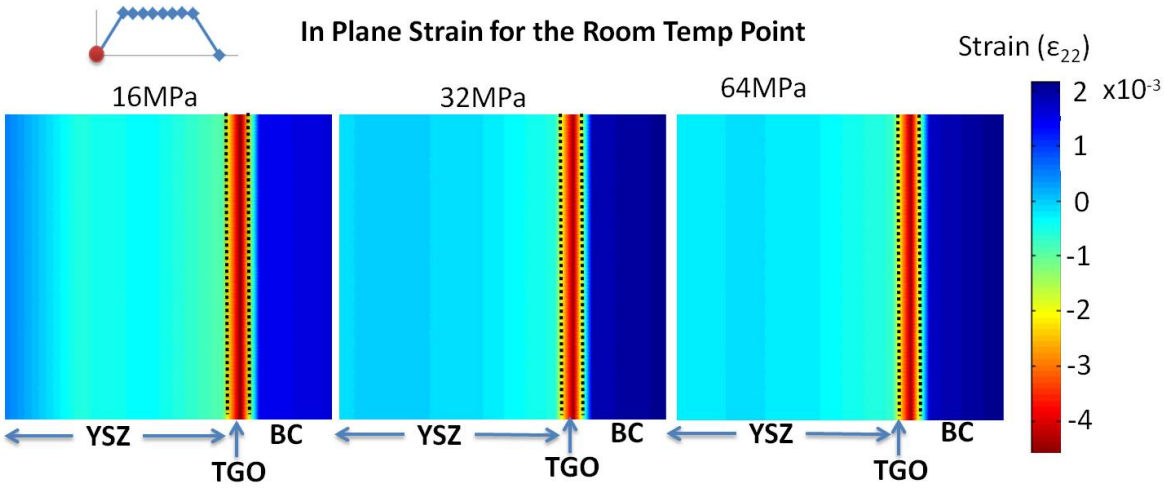

Figure 3.9: Contour plots for the room temperature point for different loads

Contour plots corresponding to the strain depth profile at the ramp-up position on the thermal cycle are illustrated in Figure 3.11. Strain in the TGO is well within the compressive region for 16MPa and 32MPa but with the increasing loading, the compressive strain reduces and at 64MPa the TGO experiences a tensile strain. This specific point in the cycle is a critical point where TGO tensile strains are observed at higher mechanical loading.

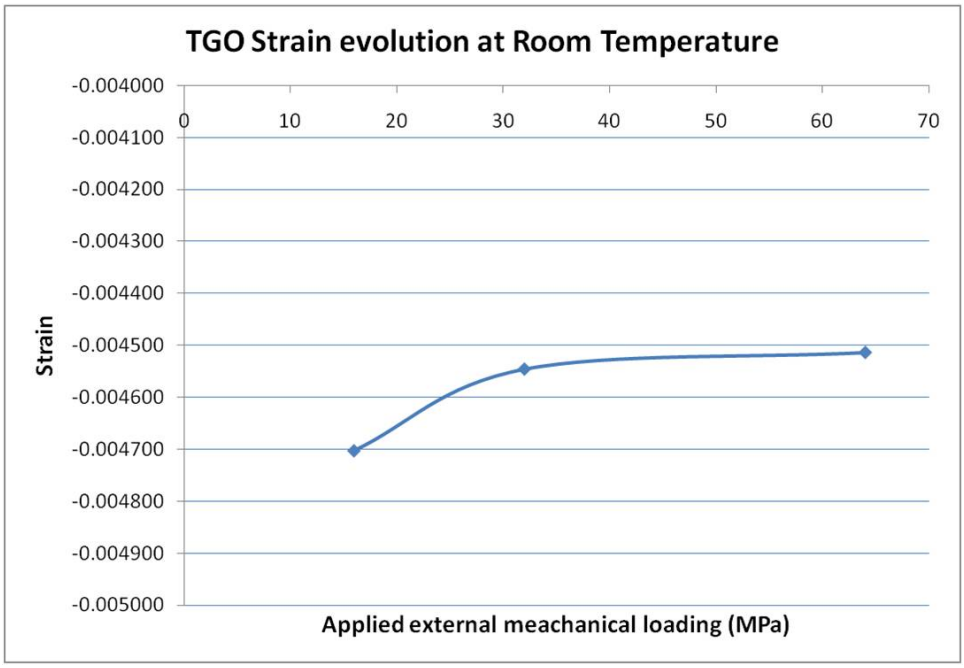

Figure 3.10: Strain evolution in the TGO layer at room temperature with the applied mechanical loads

At low loads the outer edge of the YSZ is experiencing low compressive strains and then changes towards the tensile region at the mid section of the YSZ. The trend of less compressive strains from the outer surface at high temperature has been reported in finite element analysis results presented by Limarga et al. [56]. With the variation of

loads the trend of increasing strain from the outer edge to the mid section of the YSZ is maintained. Also considering the strain at the interface between the YSZ and the TGO on the YSZ side, it was observed that these interface strains turn more tensile with increasing loads.

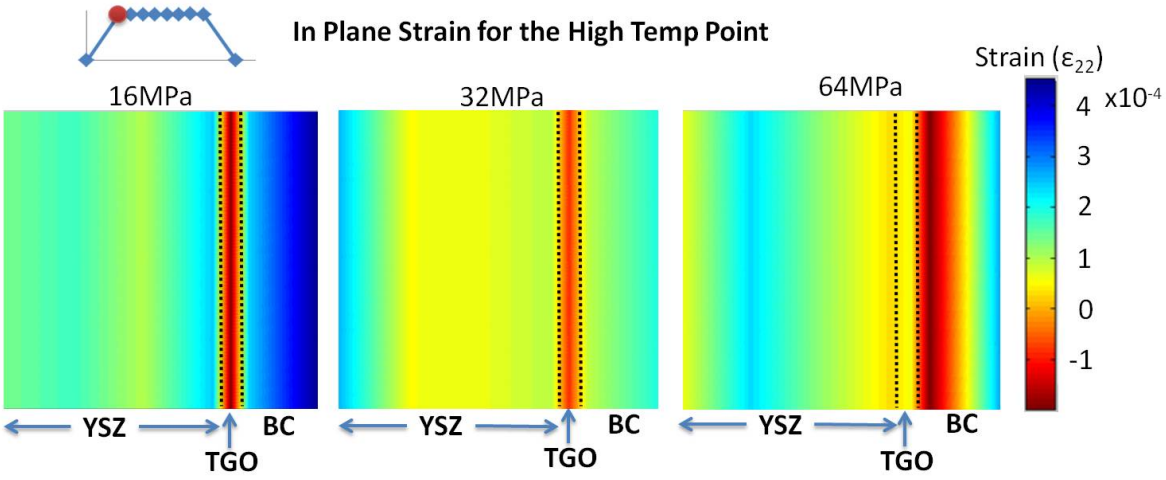

Figure 3.11: Contour plots for the ramp up point for different loads

Contour plots corresponding to the strain depth profile at the 2nd data point at high temperature on the thermal cycle is illustrated in Figure 3.12. The strain in the TGO is in the compressive region for all three loads with a greater compressive strain at 16MPa. As more evidence from Figure 3.6 points out, at 64MPa, the strain level is returning to the compressive region from the previous tensile state.

The strains on the YSZ side at the interface between the YSZ and the TGO while being under low external load were studied for the three different spots on the cycle. According to Figures 3.9, 3.11, 3.12, at room temperature the interface strain is less

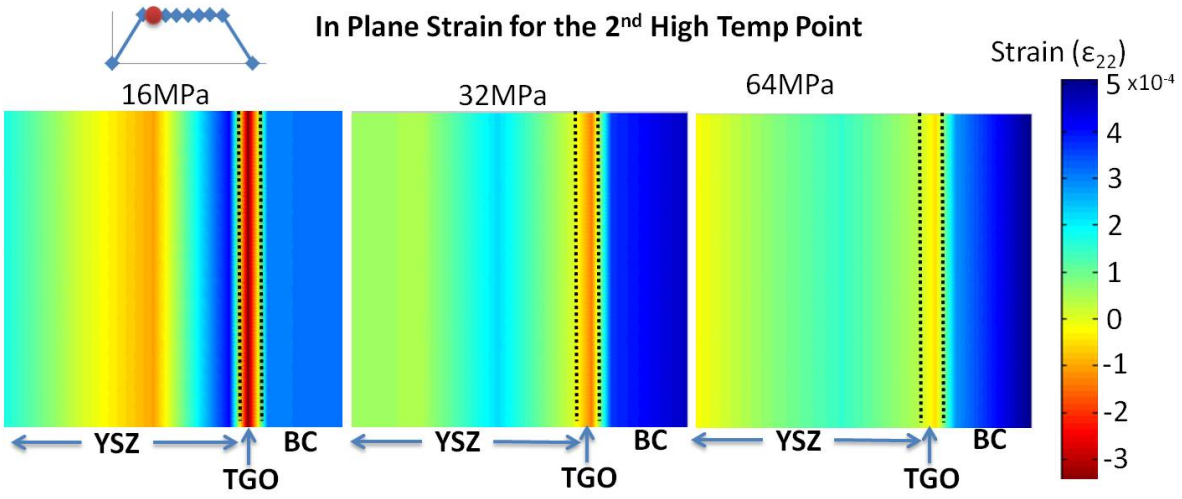

Figure 3.12: Contour plots for the 2nd point at high temperature for different loads

compressive and the strain increases to low tensile at ramp up and goes back down to be more compressive along the cycle. This behavior has been reported in numerical simulations [57].

3.4 Discussion of the findings on the overall TBC life

Results showed that the effect of increasing mechanical loads is an in-plane tensile region within the Thermally Grown Oxide (TGO) layer during a thermal cycle. This could affect the life prediction of coatings which are based on current methods neglecting mechanical loads as discussed below.

In conventional thermal fatigue tests where the mechanical loads are neglected, at high temperature, the TGO layer experiences compressive in-plane stresses while the bond coat (BC) at the BC-TGO interface experiences in-plane tensile as seen in the first contour plot in Figure 3.11. But with the mechanical loading in effect, the TGO seem to experience tensile in-plane stress while the BC-TGO interface experiences in-plane compressive as seen in the third contour plot in Figure 3.11. Due to the effect of poison's ratio, when the in-plane stress is compressive, the corresponding out-of-plane stress is tensile and vice versa for the otherwise. Our results are consistent with numerical simulations carried out by Bartsch et al. [58, 59] on a TBC system subjected to thermal gradient mechanical fatigue testing. Their results showed a tensile region in the TGO layer at high temperatures in the early cycles. This tensile region attributed as the basis of the initiation of a class of fatigue cracks observed in thermal barrier coatings (TBCs). They called this class of fatigue cracks smiley cracks when they observed them using optical microscopic means. The models they used included both non-linear and time dependent behavior, TGO growth stress, and thermo-mechanical cyclic loading and they simulated up to 50 cycles. It made evident that considering the mechanical loading induces tensile stresses within the TGO in a cycle and this is different from findings of conventional thermal studies where the stresses are generally in the compressive region. This mechanical loading effect was attributed to the failure mechanism where cracks initiated in the TGO perpendicular to the applied mechanical load and they gradually grew into the neighboring layers, the top coat and the bond coat. At the top coat these

cracks continued to be perpendicular to the applied load and this trend was also shown in In-phase thermo-mechanical tests (TMF) performed by Kitazawa et al. [34].

As shown in Figure 3.11, for higher mechanical loading condition, both the TGO layer and the top coat (YSZ) layer is experiencing a tensile in-plane strain which corresponds to a tensile in-plane stress. This could clearly be the reason for this development of the fatigue crack perpendicular to the applied load both in these layers. Also according to Bartsch et al. [58, 59], when the crack reached the bond coat from the TGO is stopped continuing perpendicular to the applied load, rather it changed its shape to be parallel to the surface creating the above mentioned smiley cracks. These cracks parallel to the surface were also observed in studies done by Evans et al. [60] and Busso et al. [61] through optical microscopic means. The reason behind this phenomenon is when the crack reaches the interface between the TGO and the bond coat it experiences an opposite state of stress from the previous where the in-plane stress is compressive and the out-of-plane stress is tensile. This would limit the vertical development of the crack and will create a tension between the two layers, BC and the TGO. The experimental measurements of the in-cycle strains under load are the first of such high-resolution in-situ data collected and the effect of these tensile strains observed on the overall life of the coating are suggested in this discussion.

Failure of the TBC coating system could occur due to many reasons. Continuously changing compositions, microstructures, interfacial morphologies, and properties of the TBC system is one of the factors. Oxidation of the bond coat which could result in

increasing growth Stress of the TGO could be another factor of TBC failure. The creep behavior of the TBC material has also been studied to investigate its effect on the failure as well [62, 63, 64]. Stress within the TBC plays an important role on the failure of the TBC as well and this research will be mainly focused on that. As shown in Figure 3.6, when the system reaches the high temperature the in-plane compressive strain which corresponds to a compressive stress takes the least possible value (or a low tensile strain which corresponds to a tensile stress for the higher mechanical loading) and it starts to reduce along the rest of the cycle making this high temperature point on the cycle the maximum stress of the system. The mean stress can be calculated as the average of this maximum stress and the minimum stress (which corresponds to the room temperature). Stephens et al. [65] showed that the effect of the mean stress on the fatigue life is such that when the mean stress increases, the number of cycles to failure decreases for a particular alternating stress. In this case, where the tensile in-plane stress was evident in the TGO is will result in a higher mean stress for the system. Therefore with the added mechanical load factor it is clear to see that it would estimate a lesser cycles to failure compared to a conventional method where the mechanical loading is neglected.

The significant finding from the thermo-mechanical experiments is represented by the strain evolution in the TGO revealing a tensile region that appears with the increasing mechanical loads. Depth resolved strains within the multiple layers were obtained at various points within the cycle providing an understanding of the changes experienced in the various layers including the interface during a thermo-mechanical cycle. The effect

of the mechanical loading was assessed based on the mean stress in the TGO and its impact on fatigue life.

CHAPTER 4
EFFECT OF MECHANICAL LOADING ON THE TGO STRESS USING PIEZOSPECTROSCOPY

4.1 Objective

As discussed in chapter 3, synchrotron XRD methods to measure the evolution of strain and subsequent analysis of stress allows for high resolution data to be collected over the cycle. This data enables the understanding of contributing factors to the overall strain distribution and effects on coating life. Such measurements have the potential to ascertain the integrity of the coatings non-invasively in an operational environment. However, the requirement of an advanced facility to achieve high energy XRD measurements indicates the need to develop a more field-applicable operational technique for integrity assessment. Photo-stimulated luminescence spectroscopy (PSLS) or Piezospectroscopy (PS), in specific when used for stress measurement, is such a method and PS measurements of stress within the oxide of various stages of cycled specimens have been related to life fraction, an early and non-invasive indicator of spallation [41, 40, 66, 67].

4.2 Theory of Piezospectroscopy

Piezospectroscopy (PS) is a non-invasive method that can be used to measure the stress within materials such as polycrystalline alumina. The photo-luminescence from chromium

(Cr^{3+}) ions within the alumina produces characteristic spectral lines also known as the R-lines when subjected to a laser excitation and the resulting spectrum is illustrated in Figure 4.1.

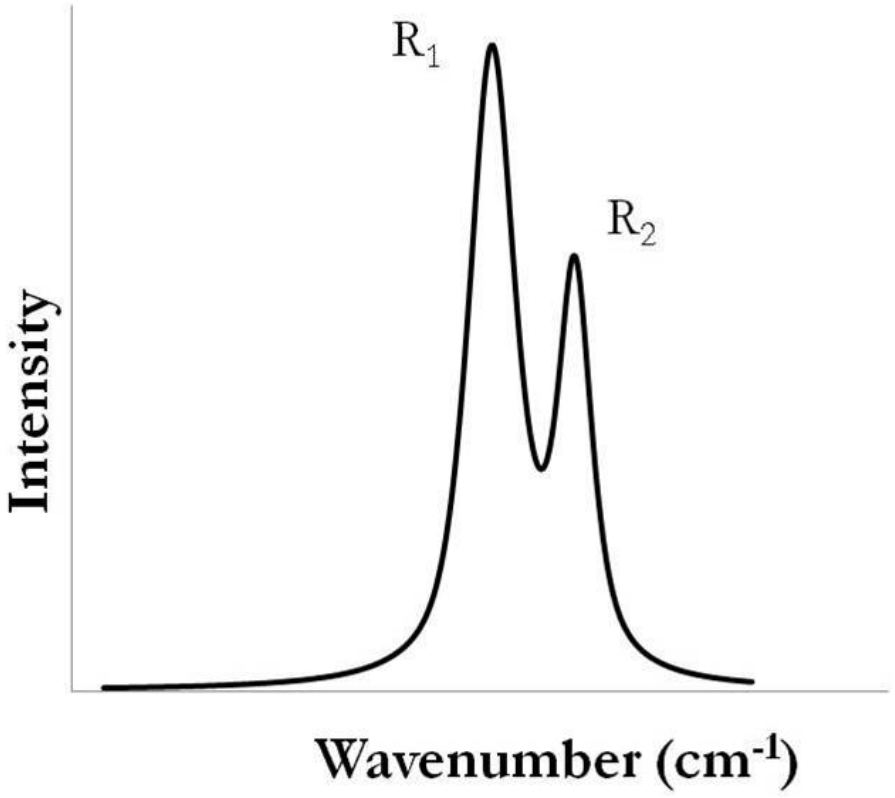

Figure 4.1: Illustration of characteristic R-lines produced

When a material experiences stress, these R-lines tend to shift due to a change in the energy of the electronic transfers [68, 69]. For a compressive stress, the shift will be towards lower wavenumbers (cm^{-1}) and for a tensile stress the shift will be towards higher wavenumbers (cm^{-1}).

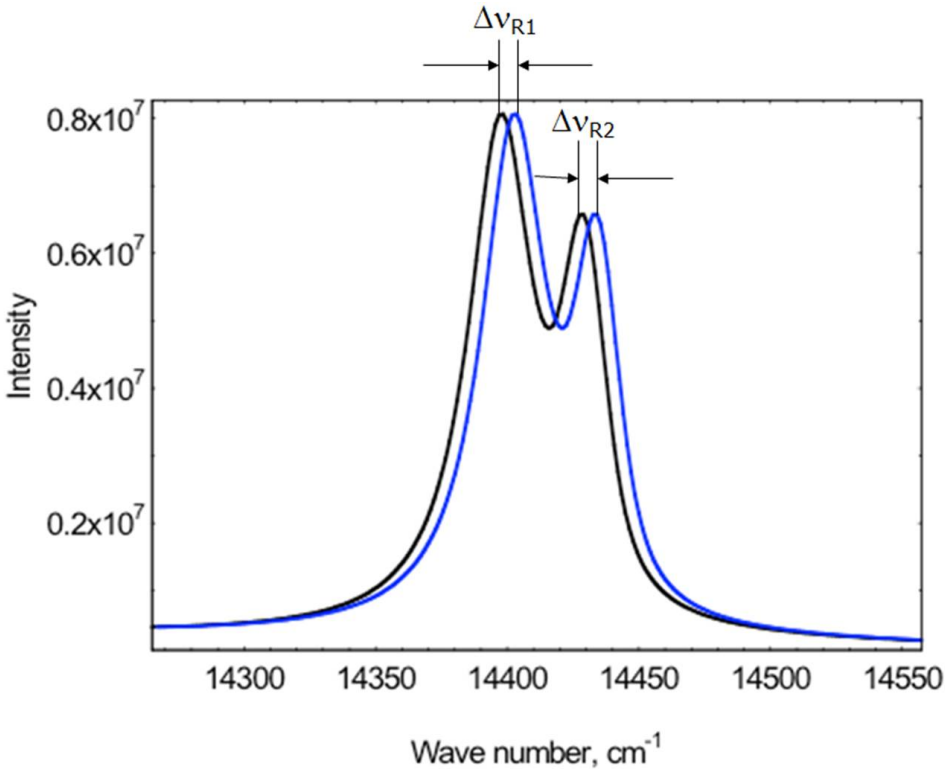

Figure 4.2: R-line shift due to stresses present in the material

The study of chromium doped alumina, has been reported by researchers over several decades from Deutschbein's [70] observation of a single Raman line at $415cm^{-1}$ to Krishnan's [71] results showing seven Raman lines. In the 1960s, ruby ($\alpha - Al_2O_3$-doped sapphire) started being considered as a laser material with studies of applications including the elucidation of the crystal field theory of ruby luminescence [72]. While studying the behavior of absorption and luminescence spectra due to uniaxial compression in Ruby, the first PS model was introduced by Kaplyanskii [73] and this effect is explained in Equation 4.1,

$$\Delta\nu = A(\sigma_1 + \sigma_2) + B\sigma_3 \tag{4.1}$$

where

$\Delta\nu$ is the frequency shift with the units cm^{-1}

σ_1, σ_2, σ_3 are the normal stresses directed along the crystallographic axes

for R1: A=-0.031, B=-0.014 with the units $cm^{-1}/\frac{kg}{mm^2}$

for R2: A=-0.027, B=-0.019 with the units $cm^{-1}/\frac{kg}{mm^2}$

A and B are parameters known today as the piezospectroscopic (PS) coefficients. This equation represents the frequency shift ($\Delta\nu$) as a linear function of stress, due to symmetry and for hydrostatic stresses this equation becomes simplified as,

$$\Delta\nu = (2A + B)\sigma \tag{4.2}$$

where

$\Delta\nu$ is the frequency shift with the units cm^{-1}

σ is the hydrostatic stress

For R1: $(2A + B)$=$7.6 * 10^{-4}$ with the units cm^{-1}/atm

For R2: $(2A + B)$=$7.3 * 10^{-4}$ with the units cm^{-1}/atm

Forman [74] used this same method in further applications where he observed the Raman shifts to analyze the hydrostatic stress in diamond anvil cells (DAC) as follows,

$$\Delta\upsilon = \pi\sigma_H \tag{4.3}$$

where

σ_H is the hydrostatic stress

π represents the PS coefficient

Grabner [75] later generalized the equation by Forman for non-hydrostatic conditions. He achieved this by using a tensorial representation for the PS coefficients and the stress components as shown in Equation 4.4.

$$\Delta\nu = \pi_{ij}\sigma_{ij} \tag{4.4}$$

where

$\Delta\nu$ is the frequency shift

π_{ij} represents the piezospectrocopic coefficient tensor

σ_{ij} is the stress state with respect to the crystallographic frame of reference.

Grabner concluded that the PS coefficients π_{ij} form a symmetric second rank tensor and therefore, σ_{ij}=σ_{ji}, however, later work by Ma and Clarke [76] dismissed the symmetry condition for the stress states and developed the following equation,

$$\overline{\Delta\upsilon} = \frac{1}{3}(\pi_{11} + \pi_{22} + \pi_{33})(\sigma_{11} + \sigma_{22} + \sigma_{33}) \tag{4.5}$$

In cases where the transverse stress is neglected ($\sigma_{33} = 0$) while assuming equal plane stresses ($\sigma_{11} = \sigma_{22} = \sigma$), these assumptions will simplify Equation 4.5 to,

$$\overline{\Delta\upsilon} = \frac{2}{3}(\pi_{11} + \pi_{22} + \pi_{33})\sigma \tag{4.6}$$

He and Clarke [77] developed the Equation 4.5 further by evaluating the coefficients of the PS tensor for a 0.05 wt% ruby by direct measurements of the frequency shift for uniaxial compression along the three principal crystallographic directions and for loading in the three principal shear directions and this modified equations for both R1 and R2 are shown below,

$$\Delta\nu\,(R_1) = 2.56\sigma_{11} + 3.50\sigma_{22} + 1.53\sigma_{33} \tag{4.7}$$

$$\Delta\nu\,(R_2) = 2.66\sigma_{11} + 2.80\sigma_{22} + 2.16\sigma_{33} \tag{4.8}$$

According to these PS coefficients, Equation 4.5 could be re-written where there will be two unknowns namely σ_{11} and σ_{22} that is when σ_{33} is assumed to be zero as shown below,

$$\Delta\nu\,(R_1) = \frac{1}{3}(7.59)(\sigma_{11} + \sigma_{22}) \tag{4.9}$$

$$\Delta\nu\,(R_2) = \frac{1}{3}(7.62)(\sigma_{11} + \sigma_{22}) \tag{4.10}$$

If equal plane stresses are assumed ($\sigma_{11} = \sigma_{22} = \sigma$), these equations will be simplified further as shown in Equations 4.11 and 4.12. These equations have been used to deter-

mine the evolution of oxide stresses in TBCs in various studies [51, 14, 78] assuming the stress state to be biaxial in the TGO.

$$\Delta\nu\,(R_1) = \frac{2}{3}(7.59)(\sigma) \tag{4.11}$$

$$\Delta\nu\,(R_2) = \frac{2}{3}(7.62)(\sigma) \tag{4.12}$$

If neither of these assumptions can be made, then there should be three or more equations to solve for the three unknowns (σ_{11}, σ_{22}, and σ_{33}) but having equations for only two distinguishable peaks (R1 and R2) demands investigating other peaks other than R1 and R2 to have three or more equations to solve for the three unknowns. To overcome this issue, Raghavan and Imbrie [79, 39] introduced the piezospectroscopic behavior of vibronic sidebands as additional peaks to be considered.

4.3 Deconvolution and Curve Fitting

Deconvolution and curve fitting is a process used on the raw R-line spectra to distinguish the two peaks.The possible noise present due to the instrumentation errors are further removed in a baseline removal process. By eliminating these errors, the most accurate peak positions and intensities for the peaks can be obtained to correctly evaluate the shifts of these peaks with stress. The deconvolution process will result in the output of two separate plots for R1 and R2 as shown in Figure 4.3.

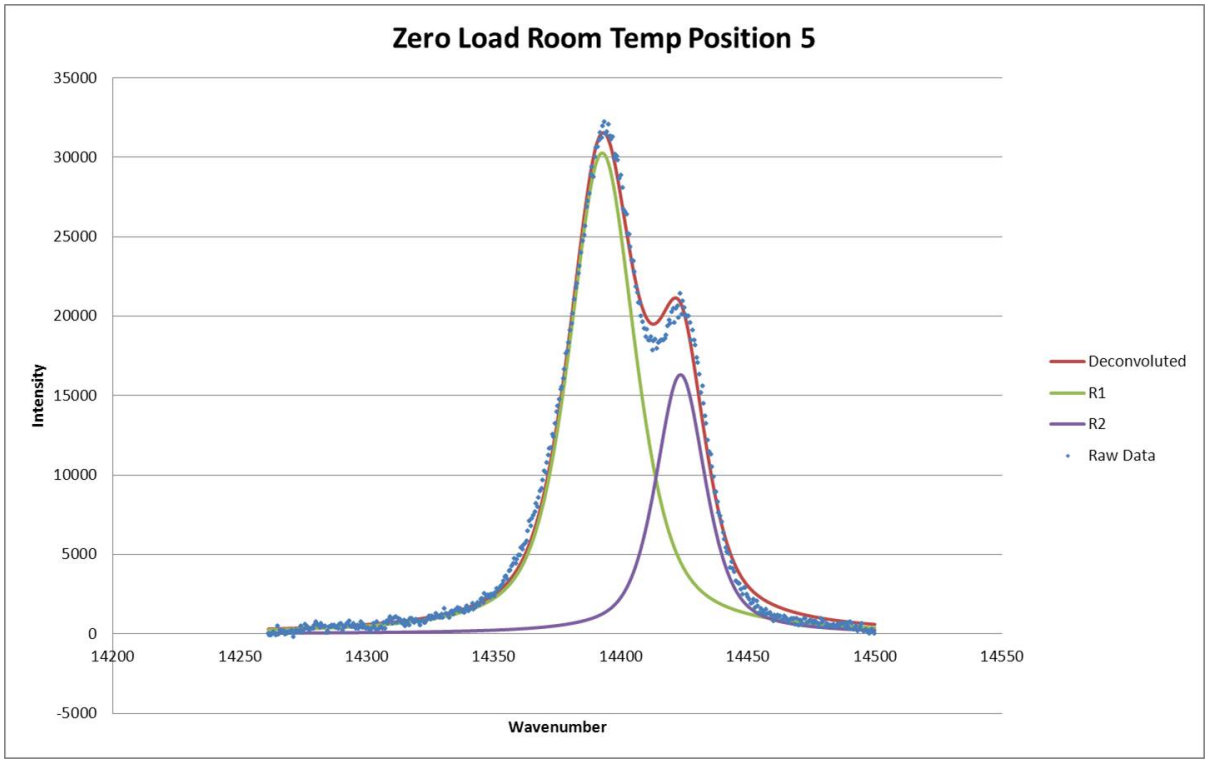

Figure 4.3: Raw data of PS deconvoluted

In the PSLS part of this research, all the raw data obtained goes through a genetic algorithm (GA) based optimization procedure for the deconvolution. This method was created and used to predict the correct peak positions for R-lines and vibronic sidebands for polycrystalline alumina by Raghavan et al. [80]. This procedure performs functions such as baseline removal, cropping, separation, and recombination to optimize the raw data on R-line spectrums. The fitting procedure used two pseudo-Voigt functions [81, 82, 83] to obtain the following design variables for each of the R1 and R2 curves: area, line-widths, peak positions, and shape factors (describing the Gaussian and Lorentzian characteristics) [66]

4.4 PSLS experimental setup

The PSLS experiments for this research took place at University of Central Florida with the use of in-house facilities such as the Renishaw RM-1000 Raman spectrometer system which was attached to a remote fiber optic laser probe system as described in Section 1.4 and a synchronized MTS Insight 50 wide load frame as shown in Figure 4.4 [43]. The same specimen from the XRD experiment was subjected to a tensile load in order to obtain values at room temperature and the stress values used were 16MPa, 32MPa and 64MPa to be consistent with the XRD experiment.

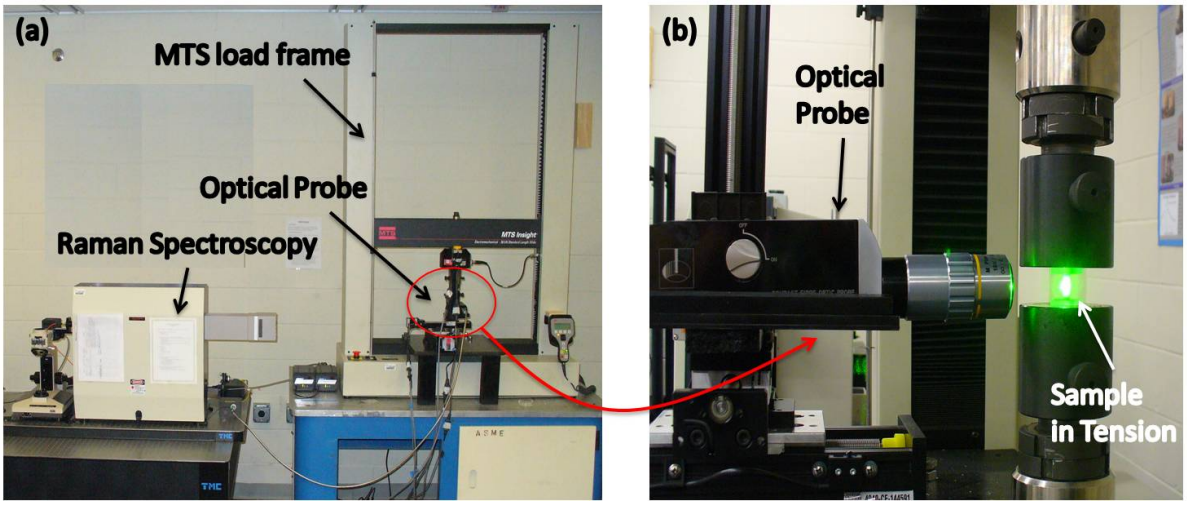

Figure 4.4: Experimental setup for the PSLS study (a) Synchronized Raman spectroscopy and the optical probe to collect data (b) Zoomed in view of the sample in the load frame during the experiment

Before using the spectrometer, calibration was required for the data to be accurate and this was achieved using a silicon (Si) sample which has a Raman spectral line at $520nm$. Following this, the TBC specimen was loaded using the MTS load frame and different loading conditions were applied. For each of these loading conditions, data was taken at three positions in the specimen as shown in Figure 4.5. For each of these positions, there were three accumulations of data for accuracy and each reading was taken under a 100% laser power, at 0.05 seconds of exposure time for a single reading. The laser used in this system was a 532nm (green) laser with 50mWpower, class 3B, requiring laser safety goggles to be used at all times [43].

4.5 PSLS results and discussion

Table 4.1 shows the results obtained for the R-line peak values for all three different loading conditions for all three different positions in the sample. These values for the three different positions were averaged and converted to stress using Equation 4.11. To convert these peak positions to stress values, a reference peak position had to be taken into consideration and for this the R-line peak values for polycrystalline alumina was used.

The reference R1peak position value for polycrystalline alumina is 14403.2 cm^{-1} and R2 value is 14433.2 cm^{-1}. The difference between these reference values and the peak position values from Table 4.1 will be used to find the biaxial stress of the TGO layer.

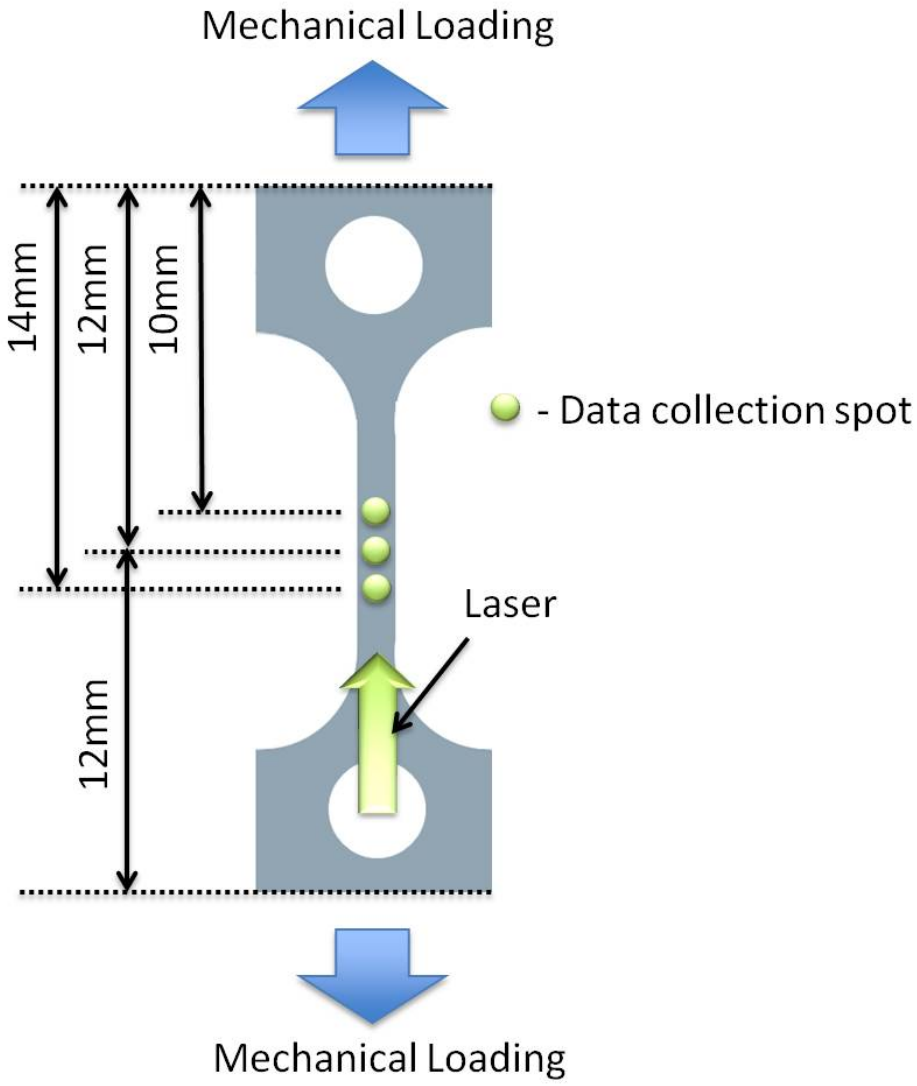

Figure 4.5: Schematic of the data collection points on the sample

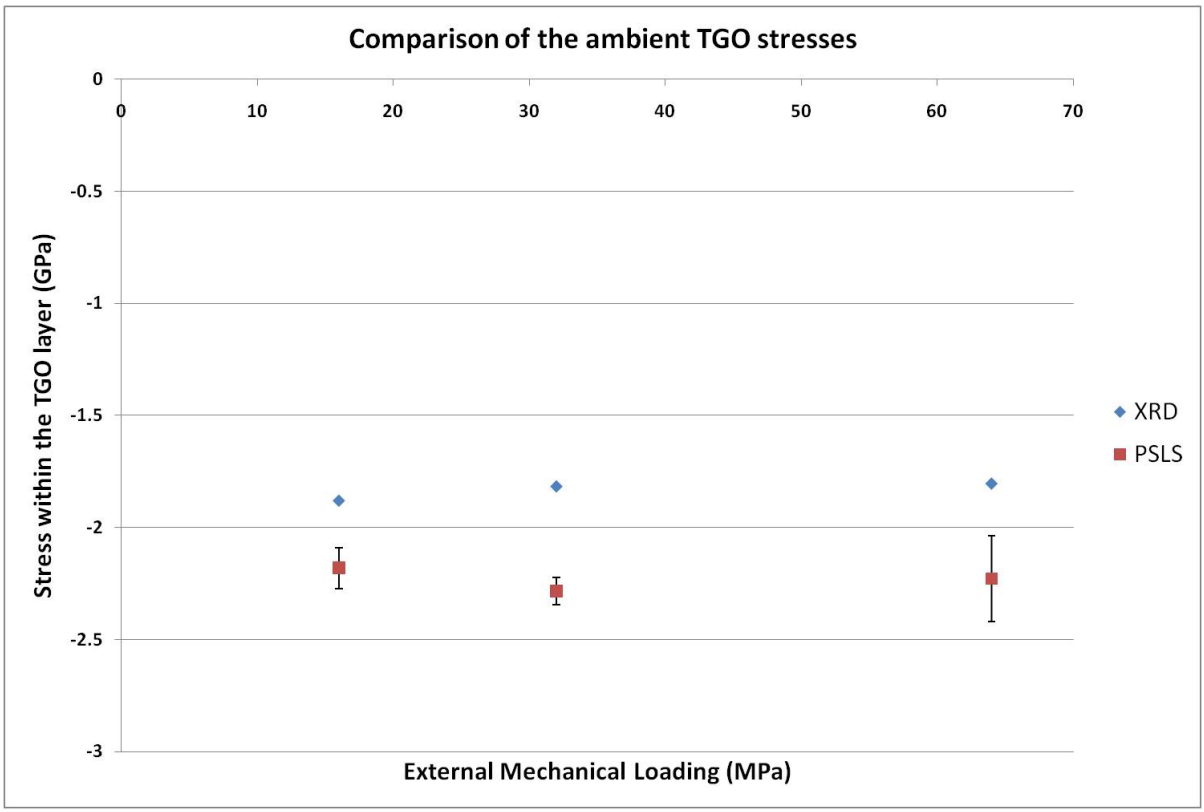

Figure 4.6: Comparison of the TGO stresses at room temperature for all three loading conditions from PSLS measurements compared with XRD measurements

Table 4.1: R-line peak values for different loading conditions

		Loading condition of the TBC specimen		
		16MPa	32MPa	64MPa
Position 1	R1	14392.4190 cm^{-1}	14391.3348 cm^{-1}	14391.9302 cm^{-1}
	R2	14423.2387 cm^{-1}	14422.1094 cm^{-1}	14422.6922 cm^{-1}
Position 2	R1	14391.5783 cm^{-1}	14391.9506 cm^{-1}	14392.8793 cm^{-1}
	R2	14422.3929 cm^{-1}	14422.7695 cm^{-1}	14423.6898 cm^{-1}
Position 3	R1	14392.4980 cm^{-1}	14391.6281 cm^{-1}	14390.9536 cm^{-1}
	R2	14423.3169 cm^{-1}	14422.4417 cm^{-1}	14421.7667 cm^{-1}

The stresses from the PSLS measurements were observed to be of the same order of magnitude as that of the XRD measurements. A distinct trend in the PSLS results with respect to the small variation in stresses caused by the externally applied mechanical loads could not be ascertained. The resolution of the PSLS method is dependent on the assumptions made initially in the analysis such as neglecting the transverse stress ($\sigma_{33} = 0$) and assuming the stress state to be biaxial ($\sigma_{11} = \sigma_{22} = \sigma$). This resolution can be improved by considering all stress states which requires additional stress-sensitive peaks to be determined and used. Future work to include the vibronic side bands that have been studied by Raghavan et al. [80] have been proposed for this purpose.

In summary, the PSLS experiments enabled a validation of the method as an operational technique that can determine the stress within the TGO. In-situ loading experiments were conducted and the stresses were confirmed to be of the same order obtained

in high resolution XRD studies. While the trend of TGO stress with mechanical load could not be confirmed due to the small variation in stresses and corresponding resolution of the PSLS method, improvements can be implemented with further studies on stress sensitive peaks from the spectra. Comparison of the PSLS method with the high resolution strain measurements from synchrotron studies is effective in assessing the improvements in resolution achieved through advances in the PS empirical model or measuring instruments.

CHAPTER 5
CONCLUSIONS

5.1 Summary of Results

The main objective of this work was to elucidate the thermo-mechanical effects on the strain evolution within an EB-PVD thermal barrier coating (TBC) using synchrotron X-ray diffraction during a thermal cycle. Both qualitative and quantitative *In-situ* data on the strain evolution under a thermal cycle with mechanical loading were obtained in this work. Systematic identification of the appropriate peaks within the multi-layer TBC system provided guidelines for future strain studies using high energy X-rays. Piezospectroscopic studies with applied mechanical loading were also addressed to be compared with the room temperature XRD data for future development of the method as an operational technique to be used outside the laboratory environment.

In-situ characterization of the strain within an EB-PVD thermal barrier coating (TBC) using Synchrotron X-ray diffraction method at sector 1-ID at the Argonne National Laboratory was presented in this work under thermo-mechanical loading. Using high energy X-rays, diffraction measurements were obtained throughout a cycle and this helped in the understanding of the evolution of the strain in the TBC system. The results complement simulation studies capturing the in-cycle behavior and enhance the limited experimental in-cycle studies. *In-situ* measurements provided high resolution quantita-

tive data on the strain evolution on the various layers of the TBC under a thermal cycle which can be used to evaluate the coating behavior and its effects on coating life.

The external mechanical loading due to the centrifugal loads which was neglected by previous studies on the strain/stress of the thermal barrier coatings was implemented in this study. Through novel experimentation including thermal and mechanical loads at the beamline, significant results were discovered on the effects of mechanical loading on the strain evolution within the thermally grown oxide layer of the TBC. Also, depth-resolved quantitative strain was presented for the various layers as contour plots over a thermal cycle highlighting the complementary strains in the adjacent layers including the bond coat and the YSZ with time and temperature. As it was pointed out in the TGO strain results, with a critical thermo-mechanical loading condition, the strain within the TGO reaches a tensile region. This has been shown experimentally through this work for the first time. These significant results contribute new findings to existing literature where purely compressive strains within the TGO have been observed with mechanical loads neglected and validates numerical thermo-mechanical studies that have been presented in the literature. This tensile strain in the TGO has been ascertained in the long run to have a negative impact on the overall life of the coating due to the effect on low cycle fatigue conditions. The findings therefore indicate the need to establish realistic testing conditions for the better understanding of coating failure to develop methods for improving their durability.

5.2 Future Work

The *in-situ* thermo-mechanical experiments using synchrotron X-ray diffraction method provided close to realistic conditions and high resolution results but there is still room for more improvements. The current study could be categorized as a Thermo-Mechanical (TM) test and this could be improved to be a Thermal gradient Mechanical (TGM) test which would replicate the real conditions of a turbine blade with internal cooling. One way to achieve this would be using tubular specimens with internal cooling implemented to create the thermal gradient representing the actual turbine blade.

Another realistic operational environment issue that these protective coatings has to face is the contamination of the TBC due to airborne sand particles. These sand particles such as volcanic ash get deposited on the TBC coating and due to the high operational temperatures these particles could melt and form calcium magnesium aluminosilicate (CMAS) contamination within the TBCs. CMAS can penetrate through the YSZ layer towards the substrate which could lead to a faster delamination of the coating. Therefore it is important to study the effect of CMAS infiltration on the TBC strain evolution during a cycle. This study could also be done with *in-situ* data collection by incorporating a particle deposition chamber in to the experimental setup in addition to the thermo-mechanical setup. Both XRD and PSLS method could serve as simultaneous characterization methods as illustrated in Figure 5.1 and a zoomed view of this schematic is elaborated in Figure 5.2

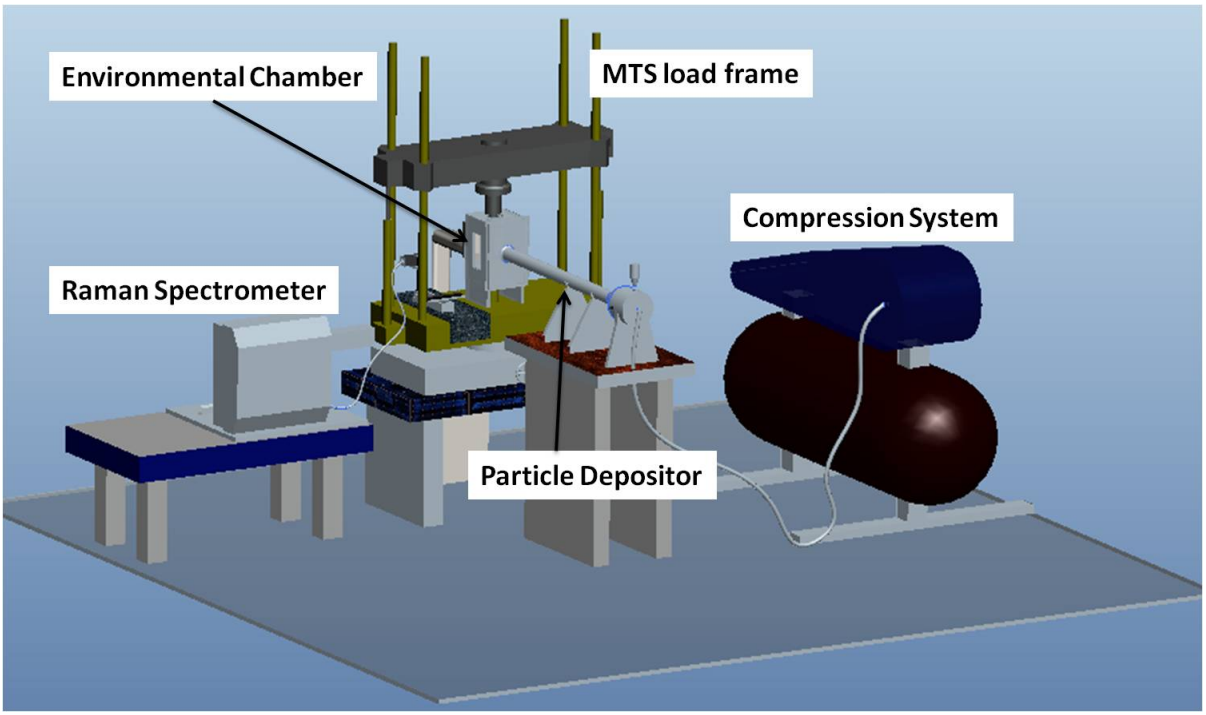

Figure 5.1: Schematic of the proposed experimental setup for *in-situ* CMAS deposition strain measurements with thermo-mechanical loading

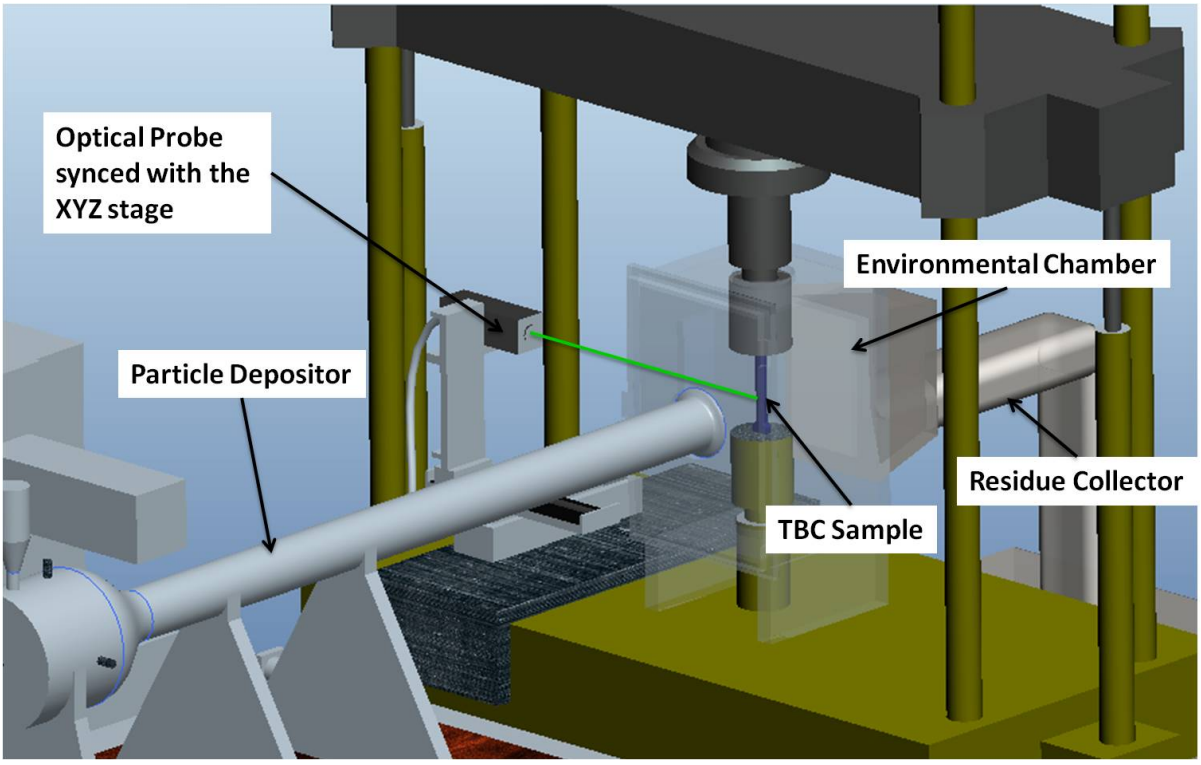

Figure 5.2: Zoomed in view of the CMAS deposition setup

Piezospectroscopic measurements were used to verify the room temperature data. This experiment could be further developed to obtain data for the complete cycle by adding a furnace to the experimental setup. Also the quality of the experimental data could be improved by improving the resolution of the data collection. More accumulations and an extended period of exposure time to the laser would improve the resolution of the data. As discussed in the section 4.5 using vibronic side bands in the spectra, which are sensitive to stress as well, could eliminate the assumption of neglecting the transverse stress ($\sigma_{33} = 0$) improving the accuracy of the results.

APPENDIX A

DIFFRACTION DATA FOR DIFFERENT MATERIALS AND COMPOUNDS

APPENDIX A
DIFFRACTION DATA FOR DIFFERENT MATERIALS AND COMPOUNDS

Table A.1: Diffraction data for $\alpha - Al_2O_3$.

2θ	d($\AA$)	I	h	k	l
25.5710	3.48068	319	0	1	2
35.1447	2.55136	720	1	0	4
37.7673	2.38	429	1	1	0
43.3443	2.08581	611	1	1	3
52.5402	1.74034	466	0	2	4
57.4894	1.60172	999	1	1	6
66.5026	1.40482	461	2	1	4
68.1911	1.37409	764	3	0	0
76.8652	1.2392	242	1	0	10
77.2244	1.23433	164	1	1	9
91.1622	1.07846	149	1	3	4
95.2221	1.04291	388	2	2	6
101.050	0.99787	279	2	1	10
116.060	0.90801	401	3	2	4

Table A.2: Diffraction data for pure Aluminum (Al)

2θ	d($\mathring{A}$)	I	h	k	l
4.344	2.338	100	1	1	1
5.018	2.024	47	2	0	0
7.099	1.431	22	2	2	0
8.325	1.221	24	3	1	1
8.692	1.169	7	2	2	2
10.04	1.0124	2	4	0	0
10.95	0.9289	8	3	3	1
11.23	0.9055	8	4	2	0
12.31	0.8266	8	4	2	2

Table A.3: Diffraction data for Centrosymmetric Boron Carbide (B_4C).

2θ	d($\mathring{A}$)	I	h	k	l
19.7145	4.49945	14	1	0	1
22.0215	4.03303	21	0	0	3
23.4984	3.78278	49	0	1	2
31.8992	2.80314	11	1	1	0
34.9561	2.56469	64	1	0	4
37.818	2.37692	100	0	2	1
53.4787	1.71199	11	2	0	5
61.7803	1.50037	9	3	0	3
63.6608	1.4605	13	1	2	5
64.5615	1.44229	10	0	1	8
66.788	1.39951	12	2	2	0

Table A.4: Diffraction data for Zirconium Yttrium Oxide.

2θ	d($\mathring{A}$)	I	h	k	l
30.1418	2.96246	998	1	0	1
34.8809	2.57005	81	0	0	2
34.9752	2.56333	136	1	1	0
43.1101	2.0966	11	1	0	2
50.2273	1.81492	340	1	1	2
50.2976	1.81255	183	2	0	0
59.6375	1.54906	119	1	0	3
59.7629	1.54611	237	2	1	1
62.6684	1.48123	59	2	0	2
73.6577	1.28503	17	0	0	4
73.8829	1.28167	45	2	2	0
81.7055	1.17759	84	0	1	0
81.8138	1.1763	41	0	0	0

Table A.5: Diffraction data for Nickel Aluminide (NiAl).

2θ	d($\mathring{A}$)	I	h	k	l
30.9821	2.884	187	1	0	0
44.3848	2.0393	999	1	1	0
55.1111	1.66508	28	1	1	1
64.5758	1.442	115	2	0	0
73.3432	1.28976	20	2	1	0
81.7221	1.17739	169	2	1	1
98.127	1.01965	42	2	2	0
106.501	0.961333	4	3	0	0
115.259	0.912001	54	3	1	0
124.707	0.869559	2	3	1	1
135.403	0.832539	13	2	2	2
148.73	0.799878	1	3	2	0

APPENDIX B

USING FIT2D TO FIND THE CALIBRATING PARAMETERS FOR DATA COLLECTION

APPENDIX B
USING FIT2D TO FIND THE CALIBRATING PARAMETERS FOR DATA COLLECTION

In the analysis of converting the diffraction patterns to radial plots to identify the peaks and consequently the strain in each peak, several initial parameters need to be found for the experiment. These parameters include sample-to-detector distance, tilt angle, rotation angle, and XY beam center on the 2D detector. These parameters are calibrated using the program Fit2D [84] with a reference material ceria Ce_2O_3 in the form of a disc. The first step is to find the beam center on the 2D detector with the first iteration and this will be further refined with multiple iterations. When the diffraction plots are read, the center is identified using three points on a ring to allow the extrapolation of the circle from these points and obtain the first iteration of the center of the beam. Then the tilt angle of the detector face and the beam will be determined by using the TILT command of the program. This corrects for any variation of perpendicularity of the detector face. These parameters are obtained by least squares fitting of powder rings. Rotation angle, on the other hand, is the offset along the azimuth. The TILT Command generates the actual tilt and rotation angle in order for fitting programs to accurately transform the plot. Once the initial iteration is run to determine the beam center, tilt angle, and the rotation angle, two or more rings will be selected to see if the first iterated values match with these. If the values do not agree with each other then more iterations are run until they come to an agreement. The CALIBRANT command was further used to fit the

powder patterns from standard calibrant material where the d-spacing values will be known from previous collected data. Using this and the initial values for the sample-to-detector distance and the wavelength a comparison will be made with the d-spacing values and the process repeated until there is an agreement. The command CAKE was then used to transform the diffraction rings in to radial plots where the horizontal axis is the radius of the ring. If the values were correct for a calibrant material which is under no stress, these radial plots are supposed to form straight lines.

APPENDIX C

ANALYSIS PROGRAMS

APPENDIX C
ANALYSIS PROGRAMS

Analysis programs were used in the peak fitting and the subsequent strain analysis of the different data files and these Matlab functions were provided by Dr. Jonathan Almer of Sector 1 within the Advanced Photon Source (APS) at the Argonne National Laboratory (ANL). The main program of this set was used to initiate the fitting sequence but it had other useful features such as plotting the raw image of the Debye-Scherer diffraction rings, the azimuthally integrated radial plot and the integrated intensity lineout plot of a single file or multiple files, etc. This program will call other programs which have the particular peak information, fitting parameters, and the calibrant information. The program fits a Pseudo-Voigt function over the azimuth of the diffraction rings and then these patterns are converted in to cartesian coordinates producing radial patterns.

LIST OF REFERENCES

[1] Nitin P. Padture, Maurice Gell, and Eric H. Jordan, "Thermal barrier coatings for gas-turbine engine applications", *Science*, vol. 296, pp. 280–284, 2002.

[2] Seetha Raghavan and Peter Imbrie, "High-resolution stress mapping of polycrytalline alumina compression using synchrotron x-ray diffraction", *Synchrotron Radiation*, vol. 18, pp. 497–505, 2011.

[3] R. O. Diaz, "In-situ stress measurements of eb-pvd thermal barrier coatings using synchrotron x-ray diffraction under thermo-mechanical loading", Master's thesis, University of Central Florida, 2010.

[4] H. Bhatnagar, S. Ghosh, and M. E. Walter, "Parametric studies of failure mechanisms in elastic EBPVD thermal barrier coatings using fem", *International Journal of Solids and Structures*, vol. 43, pp. 4384–4406, 2006.

[5] Himanshu Bhatnagar, Somnath Ghosh, and Mark E. Walter, "A parametric study of damage initiation and propagation in eb-pvd thermal barrier coatings", *Mechanics of Materials*, vol. 42, no. 1, pp. 96–107, 2010.

[6] A.G. Evans, D.R. Clarke, and C.G. Levi, "The influence of oxides on the performance of advanced gas turbines", *Journal of the European Ceramic Society*, vol. 28, no. 7, pp. 1405–1419, 2008, Developments in Ceramic Science and Engineering: the last 50 years. A meeting in celebration of Professor Sir Richard Brook's 70th Birthday.

[7] D.R. Clarke and C.G. Levi, "Materials design for the next generation thermal barrier coatings", *Annual Review of Materials Research*, vol. 33, pp. 383–417, 2003.

[8] X.Q. Cao, R. Vassen, and D. Stoever, "Ceramic materials for thermal barrier coatings", *Journal of the European Ceramic Society*, vol. 24, pp. 1–10, 2004.

[9] P. K. Wright and A. G. Evans, "Mechanisms governing the performance of thermal barrier coatings", *Current Opinion in Solid State and Materials Science*, vol. 4, pp. 255–265, 1999.

[10] Anand Kulkarni, Herbert Herman, Francesco DeCarlo, and Ramesh Subramanian, "Microstructural characterization of electron beamphysical vapor deposition thermal barrier coatings through high-resolution computed microtomography", *Metallurgical And Materials Transactions A*, vol. 35A, pp. 1945–1952, 2004.

[11] Tadeusz Hejwowski, "Comparative study of thermal barrier coatings for internal combustion engine", *Vacuum*, vol. 85, pp. 610–616, 2010.

[12] C. Giolli, A. Scrivani, G. Rizzi, F. Borgioli, G. Bolelli, and L. Lusvarghi, "Failure mechanism for thermal fatiue of thermal barrier coating systems", *Journal of Thermal Spray Technology*, vol. 18, pp. 223–230, 2009.

[13] S. R. J. Saunders, J. P. Banks, G. Chen, and C. J. Chunnilal, "Measurement of residual stress in thermally grown oxide layers in thermal barrier coating systems - development of non-destructive test methods", *Materials Science Forum*, vol. 461-464, pp. 383–390, 2004.

[14] D.R. Clarke, R.J. Christensen, and V. Tolpygo, "Evolution of oxidation stresses in zirconia thermal barrier coated superalloy leading to spalling failure", *Surface Coatings and Technology*, vol. 94-95, pp. 89–93, 1997.

[15] Catherine Guerre, Luc Remy, and Regine Molins, "Alumina scale growth and degradation modes of a tbc system", *Materials at High Temperatures*, vol. 20, pp. 481–485, 2003.

[16] P. Y. Hou, A. P. Paulikas, and B. W. Veal, "Growth strains and stress relaxation in alumina scales during high temperature oxidation", in *6th Symposium on High Temperature Corrosion and Protection of Materials*, 2004.

[17] J. A. Nychka and D. R. Clarke, "Damage quantification in tbcs by photo-stimulated luminescence spectroscopy", *Surface Coatings and Technology*, vol. 146-147, pp. 110–116, 2001.

[18] J.A. Nychka, T. Xu, D.R. Clarke, and A.G. Evans, "The stresses and distortions caused by formation of a thermally grown alumina: comparison between measurements and simulations", *Acta Materialia*, vol. 52, pp. 2561–2568, 2004.

[19] Boyd W. Veal, Arvydas P. Paulikas, and Peggy Y. Hou, "Tensile stress and creep in thermally grown oxide", *Nature Materials*, vol. 5, pp. 349–351, 2006.

[20] J. Almer, U. Lienert, R. L. Peng, C. Schlauer, and M. Oden, "Strain and texture analysis of coatings using high energy xrays", *Journal of Applied Physics*, vol. 94, pp. 697–702, 2003.

[21] J.D. Almer, G.A. Swift, J.A. Nychka, Ersan Ustundag, and D.R. Clarke, "In situ synchrotron measurements of oxide growth strains", *Materials Science Forum*, vol. 490-491, pp. 287–293, 2005.

[22] J.D. Almer and S.R. Stock, "Internal strains and stresses measured in cortical bone via high-energy x-ray diffraction", *Journal of Structural Biology*, vol. 152, pp. 14–27, 2005.

[23] R.V. Denys, A.B. Riabov, J.P. Maehlen, M.V. Lototsky, J.K. Solberg, and V.A. Yartys, "In situ synchrotron x-ray diffraction studies of hydrogen desorption and absorption properties of mg and mg-mm-ni after reactive ball milling in hydrogen", *Acta Materialia*, vol. 57, pp. 3989–4000, 2009.

[24] S.B. Yi, H.G. Brokmeier, R.E. Bolmaro, K.U. Kainer, and T. Lippmannc, "In situ measurements of texture variations during a tensile loading of mg-alloy am20 using synchrotron x-ray radiation", *Scripta Materialia*, vol. 51, pp. 455–460, 2004.

[25] M. Gelfi, E. Bontempi, R. Roberti, and L.E. Depero, "X-ray diffraction debye ring analysis for stress measurement (drast): a new method to evaluate residual stresses", *Acta Materialia*, vol. 52, pp. 583–589, 2004.

[26] K. Suzuki, K. Tanaka, and Y. Akiniwa, "Estimation of spalling stress in thermal barrier coatings using hard synchrotron xrays", *JSME International Journal*, vol. 47, pp. 318–323, 2004.

[27] J. Thornton, D. Cookson, and E. Pescott, "The measurement of strains within the bulk of aged and as sprayed thermal barrier coatings using synchrotron radiation", *Surface Coatings and Technology*, vol. 120-121, pp. 96–102, 1999.

[28] J. Thornton, S. Slater, and J. Almer, "The measurement of residual strains within thermal barrier coatings using high-energy x-ray diffraction", *Journal of the American Ceramic Society*, vol. 88, pp. 2817–2825, 2005.

[29] C. M. Weyant, J. Almer, and K. T. Faber, "Through-thickness determination of phase composition and residual stresses in thermal barrier coatings using high-energy x-rays", *Acta Materialia*, vol. 58, pp. 943–951, 2010.

[30] J. Bressers, K.Ostolaza, and M. Arana, "Coating induced life reduction of single crystal superalloy gas turbine", *Elevated Temperature Coatings: Science and Technology II*, pp. 275–285, 1996.

[31] E. Chataigner and L. Remy, "Thermomechanical fatigue behavior of coated and bare nickel based superalloy single crystals", *Thermomechanical Fatigue Behavior of Materials: Second Volume*, vol. 1263, pp. 3–26, 1996.

[32] M. Shenoy, A.P. Gordon, R.W. Neu, and D.L. McDowell, "Thermomechanical fatigue behavior of a directionally solidified ni-base superalloy", *Journal of Engineering Materials and Technology*, vol. 127, pp. 325–336, 2005.

[33] Y.H. Zhang, D.M. Knowles, and P.J. Withers, "Micromechanics of faillure of aluminide coated single crystal ni superalloy under thermomechanical fatigue", *Scripta Materialia*, vol. 37, pp. 815–820, 1997.

[34] R. Kitazawa, M. Tanaka, Y. Kagawa, and Y.F. Liu, "Damage evolution of tbc system under in-phase thermo-mechanical tests", *Materials Science and Engineering: B*, vol. 173, pp. 130134, 2010.

[35] Marion Bartsch, Bernd Baufeld, S. Dalkilic, L. Chernova, and Michael Heinzelmann, "Fatigue cracks in a thermal barrier coating system on a superalloy in multiaxial thermomechanical testing", *International Journal of Fatigue*, vol. 30, pp. 211218, 2008.

[36] J. D. Barnett, S. Block, and G. J. Piermarini, "An optical fluorescence system for quantitative pressure measurement in the diamond anvil cell", *The Review of Scientific Instruments*, vol. 44, pp. 1–9, 1973.

[37] D.R. Clarke and D.J. Gardiner, "Recent advances in piezospectroscopy", *International Journal of Materials Research*, vol. 98, pp. 1–8, 2007.

[38] Qing Ma and David R. Clarke, "Piezospectroscopic determination of residual stresses in polycrystalline alumina", *Journal of American Ceramic Society*, vol. 77, pp. 298–302, 1994.

[39] Seetha Raghavan and Peter K. Imbrie, "Ex-situ stress measurements in polycrystalline ceramics using photo-stimulated luminescence spectroscopy and high-energy x-rays", *The American Ceramic Society*, vol. 11 No. 11, pp. 1–7, 2009.

[40] J. A. Nychka, D. R. Clarke, S. Sridharan, E. Jordan, M. Gell, M. J. Lance, C. J. Chunnilall, I. M. Smith, S. R. J. Saunders, R. Pillan, V. Sergo, A. Selcuk, A. Atkinson, and K. S. Murphy, "Nde assessment of tbcs: an interim report of a photo-stimulated luminescence round-robin test", *Surface and Coatings Technology*, vol. 163-164, pp. 87–94, 2003.

[41] Swetha Sridharan, Liangde Xie, Eric H. Jordan, and Maurice Gell, "Stress variation with thermal cycling in the thermally grown oxide of an eb-pvd thermal barrier coating", *Surface Coatings and Technology*, vol. 179, pp. 286–296, 2004.

[42] Molly M. Gentleman, Vanni Lughi, John A. Nychka, and David R. Clarke, "Noncontact methods for measuring thermal barrier coating temperatures", *International Journal of Applied Ceramics Technology*, vol. 3, pp. 105–112, 2006.

[43] Gregory Freihofer, Laura Poliah, Kalippe Walker, Andre Medina, and Seetha Raghavan, "Optical stress probe: In situ stress mapping with raman and photo-stimulated luminescence spectroscopy", *Journal of Instrumentation*, vol. 5, pp. P12003, 2010.

[44] Karl U. Kainer, *Basics of Metal Matrix Composites*, Wiley-VCH, 2006.

[45] Bo Yao, Clara Hofmeister, Travis Patterson, Yong ho Sohn, Mark van den Bergh, Tim Delahanty, and Kyu Cho, "Microstructural features influencing the strength of trimodal aluminum metal-matrix-composites", *Journal of Composites: Part A*, vol. 41, pp. 933–941, 2010.

[46] Jichun Ye, Bing Q. Han, Zonghoon Lee, Byungmin Ahn, Steve R. Nutt, and Julie M. Schoenun, "A tri-modal aluminum based composite with super-high strength", *Scripta Materialia*, vol. 53, pp. 481–486, 2005.

[47] H. Natter, M. Schmelzer, M.-S Loffler, C. E. Krill, A. Fitch, and R. Hempelmann, "Grain-growth kinetics of nanocrystalline iron studied in situ by synchrotron real-time x-ray diffraction", *Journal of Physical Chemistry*, vol. 104, pp. 2467–2476, 2000.

[48] D.R. Haeffner, J.D. Almer, and U. Lienert, "The use of high energy x-rays from the advanced photon source to study stresses in materials", *Material Science and Engineering A*, vol. 399, pp. 120–127, 2005.

[49] A. Wanner and D.C. Dunand, "Synchrotron x-ray study of bulk lattice strains in externally loaded cu-mo composites", *Metallurgical and Materials Transactions A*, vol. 31A, pp. 2949–2962, November 2000.

[50] P.J. Withers, *Use of synchrotron X-ray radiationfor stress measurement*, chapter 10, pp. 170–189, Taylor & Francis, 2003.

[51] R.J. Christensen, D.M. Lipkin, and D.R. Clarke, "Nondestructive evaluation of the oxidation stresses through thermal barrier coatings using cr3+ piezospectroscopy", *Applied Physics Letters*, vol. 69, pp. 3754–3756, 1996.

[52] B. Heeg and D.R. Clarke, "Non-destructive thermal barrier coating (tbc) damage assessment using laser-induced luminescence and infrared radiometry", *Surface & Coatings Technology*, vol. 200, pp. 1298–1302, 2005.

[53] A. K. Ray, S.C. Bose, P. K. De, and D. K. Das, "Lifetime evaluation of a thick thermal barrier coated superalloy used in turbine blade", *Materials Science and Engineering*, vol. A 527, pp. 5474–5483, 2010.

[54] Huibin Xu, Shengkai Gong, and Liang Deng, "Preparation of thermal barrier coatings for gas turbine blades by eb-pvd", *Thin Solid Films*, vol. 334, pp. 98–102, 1998.

[55] ASTM, "Standard test methods for tension testing of metallic materials astm e 8/e 8m08", 2008.

[56] Andi M. Limarga, Robert Vaben, and David R. Clarke, "Stress distributions in plasma-sprayed thermal barrier coatings under thermal cycling in a temperature gradient", *Journal of Applied Mechanics*, vol. 78, pp. 011003(9 pages), 2011.

[57] R.V. Hillery, B.H. Pilsner, R.L. McKnight, T.S. Cook, and M.S. Hartle, "Thermal barrier coating life prediction model development", Tech. Rep., NASA, 1988.

[58] Mercedes T. Hernandez, Anette M. Karlsson, and Marion Bartsch, "On tgo creep and the initiation of a class of fatigue cracks in thermal barrier coatings", *Surface and Coatings Technology*, vol. 203, no. 23, pp. 3549–3558, 2009.

[59] Marion Bartsch, Bernd Baufeld, Serdar Dalkili, and Iulian Mircea, "Testing and characterization of ceramic thermal barrier coatings", *Materials Science Forum*, vol. 492-493, pp. 3–8, 2005.

[60] A.G. Evans, M.Y. He, and J.W. Hutchinson, "Mechanics-based scaling laws for the durability of thermal barrier coatings", *Progress in Materials Science*, vol. 46, pp. 249–271, 2001.

[61] E.P. Busso, L. Wright, H.E. Evans, L.N. McCartney, S.R.J. Saunders, S. Osgerby, and J. Nunn, "A physics-based life prediction methodology for thermal barrier coating systems", *Acta Materialia*, vol. 55, pp. 1491–1503, 2007.

[62] E.P. Busso, Z.Q. Qian, M.P. Taylor, and H.E. Evans, "The influence of bondcoat and topcoat mechanical properties on stress development in thermal barrier coating systems", *Acta Materialia*, vol. 57, pp. 2349–2361, 2009.

[63] D.S. Balint and J.W. Hutchinson, "An analytical model of rumpling in thermal barrier coatings", *Journal of the Mechanics and Physics of Solids*, vol. 53, pp. 949–793, 2005.

[64] P. Hanus, E. Bartsch, M. Palm, R. Krein, K. Bauer-Partenheimer, and P. Janschek, "Mechanical properties of a forged fe25al2ta steam turbine blade", *Intermetallics*, vol. 18, pp. 1379–1384, 2010.

[65] Ralph Ivan Stephens, Ali Fatemi, Robert R. Stephens, and Henry Otten Fuchs, *Metal Fatigue in Engineering*, chapter 4, pp. 61–119, Wiley-IEEE, 2001.

[66] A. Selcuk and A. Atkinson, "Analysis of the cr^{3+} luminescence spectra from thermally grown oxide in thermal barrier coatings.", *Materials Science and Engineering A*, vol. A335, pp. 147–156, 2002.

[67] Samuel Margueron, "Determination by piezospectroscopy of residual stresses in the alumina layer", in *Journee Scientifique Barrieres thermiques*, 2002.

[68] Steven E. Molis and David R. Clarke, "Measurement of stresses using fluorescence in an optical microprobe: Stresses around indentations in a chromium-doped sapphire", *Journal of Electronic Structure of Ceramics*, vol. 73, no. 11, pp. 3189 –3194, 1990.

[69] A.L. Schawlow, "Fine structure and properties of chromium fluorescence in aluminum and magnesium oxide", *Advances in Quantum Electronics*, vol. 2, pp. 50–64, 1961.

[70] Otto Deutschbein, "Die linienhafte emission und absorption der chromphosphore", *Annalen der Physik*, vol. 406, pp. 712–728, 1932.

[71] R. S. Krishnan, "Raman spectrum of alumina and the luminescence of ruby", *Nature*, vol. 160, pp. 26–26, 1947.

[72] E. Feher and M.D. Sturge, "Effect of stress on the trigonal splittings of d^3 ions in sapphire", *Physical Review*, vol. 172, pp. 244–249, 1968.

[73] A. A. Kaplyanskii and A. K. Przhevuskii, "The piezospectroscopic effect in ruby crystals", *Soviet Physics - Dokaldy*, vol. 7, no. 1, pp. 313–316, July 1962.

[74] R. A. Forman, G. J. Piermarini, J. D. Barnett, and S. Block, "Pressure measurement made by the utilization of ruby sharp-line luminescence", *Science*, vol. 176, pp. 284–285, 1972.

[75] Ludwig Grabner, "Spectroscopic technique for the measurement of residual stress in sintered al_2o_3", *Journal of Applied Physics*, vol. 49, no. 5, pp. 580–583, 1978.

[76] Qing Ma and David R. Clarke, "Stress measurement in single-crystal and polycrystalline ceramics using their optical fluorescence", *Journal of the American Ceramic Society*, vol. 76, no. 6, pp. 1433–1440, 1993.

[77] Jun He and David R. Clarke, "Determination of the piezospectroscopic coefficients for chromium doped sapphire", *Journal of American Ceramic Society*, vol. 78, no. 5, pp. 1347–1353, 1995.

[78] Maurice Gell, Swetha Sridharan, and Mei Wen, "Photoluminescence piezospectroscopy a multil purpose quality control and ndi technique for thermal barrier coatings", *International Journal of Applied Ceramics Technology*, vol. 1, no. 4, pp. 316–329, October 2004.

[79] S. Raghavan and P.K. Imbrie, "The development of photo-stimulated luminescence spectroscopy for 3d stress measurements in the thermally grown oxide layer of thermal barrier coatings", in *Proceedings of the Materials Science and Technology 2007 conference*, 2007.

[80] Seetha Raghavan, P.K. Imbrie, and William A. Crossley, "The spectral analysis of R lines and vibronic sidebands in the emission spectrum of ruby using genetic algorithms", *Applied Spectroscopy*, vol. 62, pp. 759–765, 2008.

[81] John F. Kielkopf, "New approximation to the voigt function with applications to spectral-line profile analysis", *Journal of the optical society of america*, vol. 63, pp. 987–995, 1973.

[82] G.K. Wertheim, M.A. Butler, K.W. West, and D.N.E Buchanan, "Determination of the gaussian and lorentzian content of experimental line shapes", *Review of Scientific Instruments*, vol. 45, pp. 1369–1371, 1974.

[83] T. Ida, M. Ando, and H. Toraya, "Extended pseudo voigt function for approximating the voigt profile", *Journal of Applied Crystallography*, vol. 33, pp. 1311–1316, July 2000.

[84] A. P. Hammersley, "European synchrotron research facility (esrf), internal report. esrf98ha01t, fit2d v9.129 reference manual v3.1.", Tech. Rep., ESRF, Grenoble, France, 1998.